von Karman Institute for Fluid Dynamics

Lecture Series 2003-04

POST-PROCESSING OF EXPERIMENTAL AND NUMERICAL DATA

February 17-21, 2003

TWO TYPICAL APPLICATIONS OF POD: COHERENT STRUCTURES EDUCTION AND REDUCED ORDER MODELLING

L. Cordier & M. Bergmann
LEMTA, France

Two typical applications of POD: coherent structures eduction and reduced order modelling.

Cordier Laurent & Bergmann Michel
Laboratoire d'Energétique et de Mécanique Théorique et Appliquée
UMR 7563 (CNRS - INPL - UHP)
ENSEM - 2, avenue de la Forêt de Haye
BP 160 - 54504 Vandoeuvre Cedex, France

Contents

The first lecture notes (see Cordier and Bergmann, 2002) were devoted to an overview of the Proper Orthogonal Decomposition (POD). POD was first introduced as an approximation method whose solutions are given by a truncated Singular Value Decomposition (SVD). Therefore, the connections between SVD and POD were particularly emphasized. Then, the two main POD approaches: classical POD and snapshot POD were described in details and the relationships between POD modes and coherent structures (CS) discussed. Finally, it was clearly demonstrated that the Proper Orthogonal Decomposition generalized the classical Fourier analysis to inhomogeneous directions.

In this companion paper, we consider two typical applications of POD: coherent structures identification and model reduction aspects (see the introduction of Cordier and Bergmann, 2002 for a general discussion). The Proper Orthogonal Decomposition can first be viewed as a particular data processing technique that extracts, from experimental data or detailed simulations of high dimensional systems, "mode shapes" or basis functions assimilated to CS. This viewpoint is illustrated in part I where the Proper Orthogonal Decomposition is used to educe[1] CS in a three-dimensional plane turbulent mixing layer simulated by Large Eddy Simulation (LES). However, up to now, this approach of POD is too restrictive because it has a purely descriptive nature. Clearly, our understanding of the rôle of CS in turbulence generation could be improved, if we could derive models as simple as possible that mimic the dynamical behaviour of the flow. One of the methods is to combine the POD basis functions previously determined and Galerkin projections to yield low-dimensional dynamical models. This procedure, that has already been employed, with success, to study either the near-wall evolution of the flow within a turbulent boundary layer (see Aubry *et al.*, 1988) or the dynamical evolution of a plane mixing layer (see Ukeiley *et al.*, 2001), is applied in part II to the cylinder flow. In this part, we show that POD reduced order models can be very efficient for low-cost numerical simulations of the Navier-Stokes equations that can be used to solve optimization and control problems in unsteady flows.

[1]Some of the material presented in part I is excerpted from two conference papers written by one of the author (LC) and previous co-workers (see Cordier*et al.*, 1997; Lardat *et al.*, 1997b and the acknowledgements in §5).

Part I
Coherent structures eduction

1 Introduction

The objective of this part is to demonstrate for a basic free turbulent flow that the Proper Orthogonal Decomposition (see Cordier and Bergmann, 2002) can be used to identify the CS embedded inside the overall chaotic behaviour of the turbulence field. These large-scale coherent structures, which contain most of the turbulent kinetic energy, are mainly responsible for mixing, vibrations, radiated noise, etc... Therefore, our ability to describe correctly the characteristics of these structures, and eventually to predict[2] precisely their time evolution, can greatly contribute to our understanding of turbulent flows and is a capital point for active flow control[3]. In the POD approach, the coherent structures are defined in terms of optimal signature of the turbulent kinetic energy and they are simply associated to the POD eigenfunctions.

In the following, the POD is applied on the results of the Large Eddy Simulation (LES) of a three-dimensional, plane mixing layer spatially developing downstream of a flat plate. The LES is performed on the same flow configuration studied experimentally in details by Delville (1994, 1995). This numerical approach complete earlier works dedicated to the study through combined use of experimental data obtained by rakes of hot-wires and POD of the spatial organization and temporal evolution of the CS present in the flow (see Delville *et al.*, 1999 and Ukeiley *et al.*, 2001 respectively).

An outline of the contents of this part is now given. To begin, the numerical approach used in the LES of the plane mixing layer is extensively described in §2. Then, in order to reduce the data storage requirements, a data compression procedure based on scalar PODs is applied to the three components of the velocity (§3). The scalar POD is presented in §3.1 and the applications to the data-base generated by the LES are done in §3.2. Due to the energetic optimality of the POD basis functions, it is shown in

[2]The development of low-order dynamical systems based on POD is not adressed in this part but is postponed in part II.

[3]The active control of fully developed turbulent flows are of particular interest for many industrial configurations. For example, in aerodynamic applications, the control and modification of turbulent flows could be used either in external flows, to reduce the total drag of aerospace vehicules or in internal flows, to increase the mixing rate in a scramjet for instance.

§3.2.1 that only 10% of the POD modes obtained by the scalar-PODs are necessary to rebuild accurately the flow realizations. The contribution of the 200 first spatial eigenfunctions to the two-point space correlations is then estimated by comparison to the correlations experimentally determined by Delville (1995). Very good agreements are achieved (see §3.2.4). Therefore we conclude that the spatial eigenfunctions determined in §3.2.2 by use of the scalar PODs mimic very well the coherent structures organization. Finally, using the filtered data, a three-dimensional snapshot POD described in §4.1 is performed. The spatial organization of the eigenfunctions determined by the snapshot POD are found in good agreement with the experimental coherent structures (see §4.2.2).

2 Large Eddy Simulation of the plane mixing layer

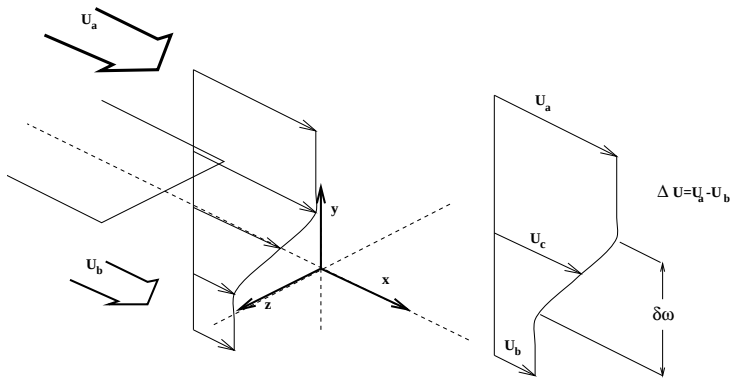

Figure 1: Coordinates and notations for the three-dimensional plane mixing layer.

The velocity ratio is $r = U_b/U_a = 0.59$, where $U_a = 42.8$ m/s and $U_b = 25.2$ m/s are the magnitudes of the external velocities of the boundary layers at the trailing edge of the flat plate (see figure 1). The Reynolds number, based on δ_{ω_0} and on $\Delta U = U_a - U_b$, is 35000 where δ_{ω_0} refers to the experimental vorticity thickness at a prescribed location, $\delta_{\omega_0} = 30 \times 10^{-3}$ m.

2.1 Numerical approach

2.1.1 Governing equations

The LES of the mixing layer is performed using the filtered Navier-Stokes equations by means of the Reynolds decomposition. Using the velocity-vorticity formulation, these equations are written as follows:

$$\begin{aligned} \frac{\partial \underline{\vec{\omega}}}{\partial t} - \vec{\nabla} \times (\underline{\vec{v}} \times \underline{\vec{\omega}}) &= -\frac{1}{Re} \vec{\nabla} \times \vec{\nabla} \times \underline{\vec{\omega}} + \vec{\nabla} \times \vec{\tau} \\ \underline{\vec{\omega}} &= \vec{\nabla} \times \underline{\vec{v}} \\ \vec{\nabla} \cdot \underline{\vec{v}} &= 0 \end{aligned} \tag{1}$$

where Re is the Reynolds number ($Re = \dfrac{U_a \theta_a}{\nu}$), based on the external velocity U_a of the high speed boundary layer and its momentum thickness θ_a. In these equations, $\underline{\vec{v}}$ is the resolved-part (filtered part) of the velocity field, $\underline{\vec{\omega}}$ is its rotational field and $\vec{\tau}$ stands for the subgrid scale contribution: $\vec{\tau} = \underline{\vec{v} \times \vec{\omega}} - \underline{\vec{v}} \times \underline{\vec{\omega}}$.

2.1.2 Subgrid scale models

In order to take into account the participation of the small-scale structures in the fluid motion, the subgrid scale vector $\vec{\tau}$ is modeled using the vorticity transfer theory of Taylor (1932), by means of an eddy viscosity ν_t : $\vec{\tau} = -\nu_t \, \vec{\nabla} \times \underline{\vec{\omega}}$. In many subgrid scale models, the eddy viscosity is often related to the local vorticity. Hence, these models give subgrid contribution even in laminar flows which does not correspond to the right behaviour. The idea sought after in the *mixed-scale model* (see Ta Phuoc, 1994; Sagaut, 1995) is to dump smoothly the eddy viscosity ν_t in the regions where all the eddy structures are well captured. Using the *mixed-scale model*, ν_t is then calculated using two different velocity scales.

2.1.3 Computational domain and grid

The computational domain starts at the trailing edge of the flat plate and spreads over $L_x = 20 \; \delta_{\omega_0}$ far downstream. The size of the mesh is $401 \times 71 \times 55$. The grid uses $N_x = 401$ points equally spacing in the streamwise direction (x). In the inhomogeneous (vertical) direction (y), the domain lays over $L_y = 6 \; \delta_{\omega_0}$. The mesh is tightened around the centerline of the mixing layer, following a cosine distribution using $N_y = 71$ grid-points. The flow is supposed to be periodic in the spanwise direction (z) ; the domain lays

over $L_z = 5\ \delta_{\omega_0}$ using $N_z = 55$ points equally spaced. Using this mesh, the grid filter width ($\underline{\Delta} = (\Delta x \times \Delta y \times \Delta z)^{1/3}$) is close to the Taylor micro-scale estimated following the experimental results (see Delville, 1995).

2.1.4 Boundary conditions

Since a staggered grid is used at the inflow surface defined as the trailing edge of the splitting plate ($x = 0$), we need to prescribe the value of the normal component of the mean velocity $\underline{v_x}$ and the mean vorticity tangential components ($\underline{\omega_y}$, $\underline{\omega_z}$). $\underline{v_x}$ is initialized using two turbulent Whitfield profiles, for the boundary layers from each side of the flat plate. The profiles of $\underline{\omega_y}$ and $\underline{\omega_z}$ are then deduced from $\underline{v_x}$ profiles. A white noise is superimposed on $\underline{\omega_y}$, $\underline{\omega_z}$. The perturbation magnitude is equivalent to an amplitude of $10^{-3}\ U_a$ on the streamwise velocity component $\underline{v_x}$. At the outlet boundary ($x = 20\ \delta_{\omega_0}$), the tangential components of the vorticity are calculated by extrapolation along the characteristic directions. The normal component of the velocity $\underline{v_x}$ is then deduced from the vorticity profiles, prescribing that the mass conservation is satisfied. At the upper and lower surfaces of the domain ($y = \pm 3\ \delta_{\omega_0}$), slip conditions are imposed: $\underline{v_y} = 0$ and $\frac{\partial \underline{v_x}}{\partial y} = 0$, $\frac{\partial \underline{v_z}}{\partial y} = 0$.

2.1.5 Method of resolution

The spatial discretization uses a MAC staggered grid where the velocity components are defined at the center of the cell faces, the vorticity components are prescribed at the middle of the vertices and the pressure as well as the eddy viscosity are defined at the center of the cell. The system of equations (1) is solved in two steps (see Lardat *et al.*, 1997a). First we solve the transport equation of the vorticity. The time discretization uses a Crank-Nicholson scheme. The convective terms are estimated by means of an Adams-Bashforth extrapolation which is 2^{nd} order accurate in time. The space discretization uses a 2^{nd} order finite difference method by means of a QUICK scheme for the convective terms and a centered scheme for the diffusive ones. The vectorial Helmholtz problem, arising from the vorticity transport equations, is solved with a block Jacobi iterative algorithm. Secondly, we solve the Cauchy-Riemann problem. Knowing the new vorticity field $\underline{\vec{\omega}}^{n+1}$, the velocity field is solved using a projection (or fractional step) method, following the work made by Bertagnolio and Daube (1996). In the first step, an intermediate velocity field is obtained which satisfies the curl

equation ($\vec{\boldsymbol{\nabla}} \times \vec{\boldsymbol{v}} = \vec{\boldsymbol{\omega}}$). This intermediate velocity is then projected onto the space of divergence free vector fields (see Bertagnolio and Daube , 1996; Lardat *et al.*, 1997a).

2.2 Validations of the numerical simulation

A portion of the computational domain has been selected to compare the mean and Reynolds stress profiles obtained with the results of the numerical simulation to the experimental data described in Delville (1995). This region starts from 10 δ_{ω_0} downstream of the trailing edge of the flat plate and lays over 5 δ_{ω_0} to minimize the influence of the exit boundary condition. The average has been calculated over a dimensionless time $T = 206$ (where T is based on U_a and δ_{ω_0}) and by integrating in the spanwise direction:

$$< . >= \frac{1}{L_z T} \int_{L_z} \int_{T} . \, dt \, dz$$

The self-similarity behaviour is recovered by the LES ; the vorticity thickness δ_ω and its longitudinal evolution $d\delta_\omega/dx$ are correctly predicted by the computation (LES: $d\delta_\omega/dx = 4.22\ 10^{-2}$; Experiments: $d\delta_\omega/dx = 4.1\ 10^{-2}$). Very good agreements are achieved on the profiles of the Reynolds stress components (see Lardat *et al.*, 1997b). As regards the instantaneous organization of the mixing layer, we plot on figure 2 the isobaric surface of the pressure field at a threshold $\underline{p} - P_0 = -10^{-3}$ for a dimensionless time $t = 250$. The large scale arrangement, strongly tridimensionnal, is clearly visible on this figure. A streamwise length scale has been recorded close to $\Lambda_x \sim 3.25\ \delta_\omega$. In the spanwise direction (z), two large scale patterns have been recorded leading to an estimation of the spanwise length-scale close to $\Lambda_z \sim 2/3\Lambda_x$, which is in rather good agreement with the one generally admitted (see Bernal and Roshko, 1986).

3 Data compression procedure: scalar-PODs approach

3.1 Motivations and description of the method

In order to reduce the data storage requirements[4], a data compression procedure is used. This compression is based on a scalar version of the "classical"

[4]Assume that the results obtained by the LES (three velocity components plus the pressure field) are stored in double precision, then the total volume necessary to store $N_t = 1000$ time steps is equal to $N_x \times N_y \times N_z \times N_t \times 4 \times 8$ bytes $\simeq 50$ Gigabytes.

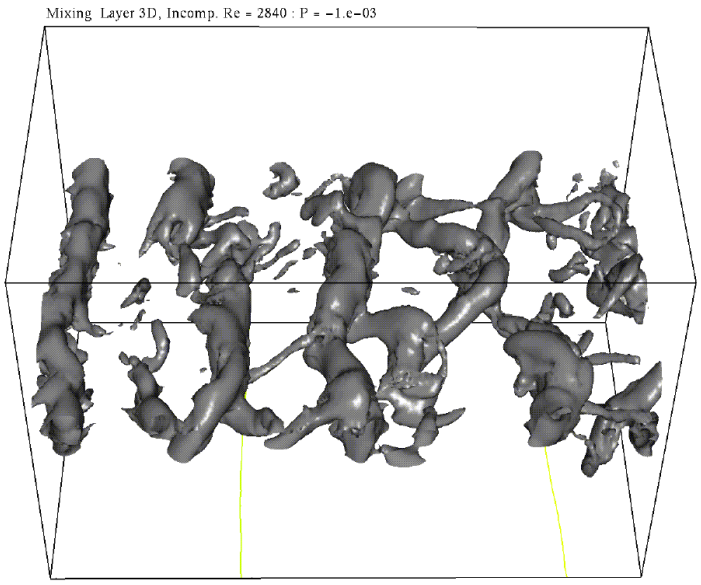

Figure 2: Isobaric surface of the instantaneous calculated pressure field at a dimensionless time t = 250. (region clipped: $10\,\delta_{\omega_0} < x < 20\,\delta_{\omega_0}$).

POD (see Cordier and Bergmann, 2002, §5.3). The principle is to retain only "relevant" POD modes to rebuild the flow realizations that are used later in the snapshot POD analysis of §4. In this approach, we express each component of the fluctuating velocity $\widetilde{v}_i(\vec{\boldsymbol{x}},t)$, $i = 1,2,3$ in terms of spatial POD basis functions ϕ_i depending only on the x and y directions:

$$\widetilde{v}_i(\vec{\boldsymbol{x}},t) = \sum_{n=1}^{N_{POD}} a_i^{(n)}(z,t)\ \phi_i^{(n)}(x,y) \tag{2}$$

where:

$$v_i(\vec{\boldsymbol{x}},t) = < v_i > (x,y) + \widetilde{v}_i(\vec{\boldsymbol{x}},t) \tag{3}$$

and

$$< v_i > (x,y) = \frac{1}{T\ L_z} \int_T \int_{L_z} v_i(x,y,z,t)\ dt\ dz\ . \tag{4}$$

For this scalar-POD, the integral Fredholm equation which is solved, writes[5]:

$$\int_{L_x} \int_{L_y} R_{jj}(x,y,x',y')\ \phi_j^{(n)}(x',y')\ dx'\ dy' = \lambda_j^{(n)}\ \phi_j^{(n)}(x,y) \tag{5}$$

[5]No implicit summation over the subscript j.

where the velocity correlations $R_{jj}(x,y,x',y')$ are calculated from the LES results using the following relationship:

$$R_{jj}(x,y,x',y') =< v_j \cdot v_j > (x,y,x',y') - < v_j > (x,y) \cdot < v_j > (x',y') \quad (6)$$

The space-time coefficients $a_i^{(n)}(z,t)$ are then evaluated by projection of the flow realizations onto the spatial POD basis functions:

$$a_i^{(n)}(z,t) = \int_{L_x} \int_{L_y} \widetilde{v_i}(x,y,z,t).\phi_i^{(n)}(x,y)\, dx\, dy \quad (7)$$

where these expansion coefficients verified the orthogonality relationship:

$$\frac{1}{L_z T} \int_T \int_{L_z} a_i^{(n)}(z,t).a_i^{(m)}(z,t)\, dz\, dt = \lambda_i^{(n)} \delta_{nm} \quad (8)$$

Hereafter, among the $N_{POD} = N_x \times N_y$ modes resulting from each scalar-PODs (5), only $N^{KL} \ll N_{POD}$ modes are retained to rebuild the flow realizations $\widetilde{v_i}$. By definition (see Sirovich, 1987a), the Karhunen-Loève dimension N^{KL} is the minimum number of POD modes necessary to represent the total turbulent energy initially contained in the flow with an accuracy better then 99%. This dimension is closely[6] related to the relative information content of the POD basis functions defined by equation (9) and used later in §8.4.1 to determine how many POD modes need to be kept in the low-dimensional system.

By this way, instead of storing $N_x \times Ny \times Nz \times N_t \times 3$ floating point numbers, we just need to store $N_z \times N_t \times N^{KL} \times 3$ numbers to describe the temporal history of the three-dimensional flow field.

3.2 Application of the scalar-PODs

The scalar-POD approaches are applied on the fluctuating velocity field $\widetilde{v_i}(\vec{\boldsymbol{x}},t)$ provided by the numerical simulation. The POD analysis is performed on $N_t = 1000$ temporal events representing a dimensionless time close to $T = 17$. We apply the scalar-PODs on a box with a streamwise extent of $10\delta_{\omega_0}$. In practice, knowing an initial state, we have first run the calculation on 1000 time steps to calculate the spatial velocity correlations $R_{jj}(x,y,x',y')$ from equation (6). Secondly, the integral eigenvalue problem (5) has been solved for $j = 1,2,3$. Finally, the numerical simulation has been re-run from the same previous initial state to determine via equation (7) the space-time coefficients $a_i^{(n)}(z,t)$.

[6] To be more precise, in the context of POD reduced order models, N^{KL} corresponds to the smallest integer M such that the information content $RIC(M)$ defined by (69) is greater than $\delta\,\%$ with $\delta = 99$.

3.2.1 Scalar-PODs convergence

In a similar way as what has been done for the Singular Value Decomposition (see Cordier and Bergmann, 2002, §3.6), the convergence of the scalar-POD is represented by the relative information content of the POD basis functions. This quantity, represented in figure 3, is defined as the ratio between the energy contained in the first n POD modes and the turbulent kinetic energy in the flow:

$$RIC(n) = \frac{\sum_{i=1}^{n} \lambda^{(i)}}{\sum_{i=1}^{N_{POD}} \lambda^{(i)}} \tag{9}$$

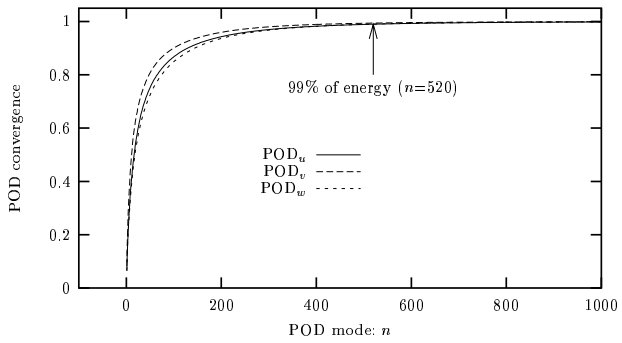

Figure 3: Relative information content for the scalar-PODs.

The convergence is relatively rapid since about 57% of the turbulent kinetic energy is contained within the 20 first modes and the first 520 modes contain 99% of the turbulent kinetic energy. One can note that a large compression ration (90%) is obtained: $N_x N_y / N^{KL} \simeq 10$.

3.2.2 Spatial eigenfunctions

In figures 4, 5 and 6 are represented in the plane (x, y), iso-contours of the u, v and w component respectively of $\phi_i^{(n)}(x, y)$ for four selected modes (modes 1, 2, 20, 200). In these figures, the lines in bold correspond to positive values while the thin ones correspond to negative values. Considering these eigenfunctions, one can notice a streamwise shift when comparing modes 1 and 2. Whatever the velocity components are, the mode 2 is shifted downstream when compared to mode 1. This behaviour, explained by the convective nature of the flow (see Rempfer and Fasel, 1994), is common to many POD

applications. Therefore, the same pattern was encountered for the cylinder flow studied in part II and further explanations can be found in §8.3.2. All these POD eigenfunctions exhibit a preferred organization ; for low-order modes, this organization follows the longitudinal expansion of the mixing layer (see figures 4, 5 and 6). However, compared to these low-order modes, the high-order modes are more tightened in the vicinity of the centerline of the mixing layer and correspond, as expected, to smaller spatial length scales.

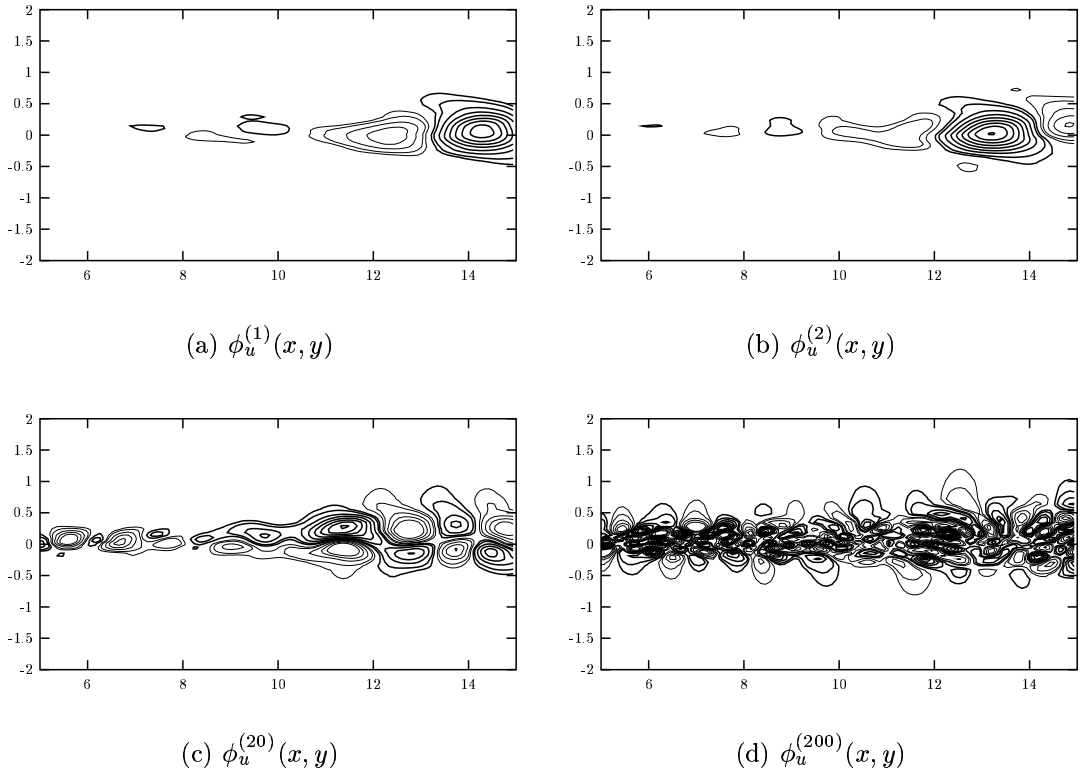

(a) $\phi_u^{(1)}(x,y)$ (b) $\phi_u^{(2)}(x,y)$

(c) $\phi_u^{(20)}(x,y)$ (d) $\phi_u^{(200)}(x,y)$

Figure 4: Iso-contours of the spatial eigenfunctions $\phi_u^{(n)}(x,y)$ obtained from the scalar-POD applied to the velocity component u ($n = 1, 2, 20$ and 200).

3.2.3 Expansion coefficients

The time histories of the first four expansion coefficients $a_i^{(n)}(z,t)$ obtained via equation (7) for the scalar-PODs on u, v and w are plotted in figure 7, on the middle z-plane $z = z_0$. A time shift is visible between $a^{(1)}(z_0,t)$ and $a^{(2)}(z_0,t)$ and between $a^{(3)}(z_0,t)$ and $a^{(4)}(z_0,t)$ for all the velocity components. This behaviour has to be related to the streamwise shift already no-

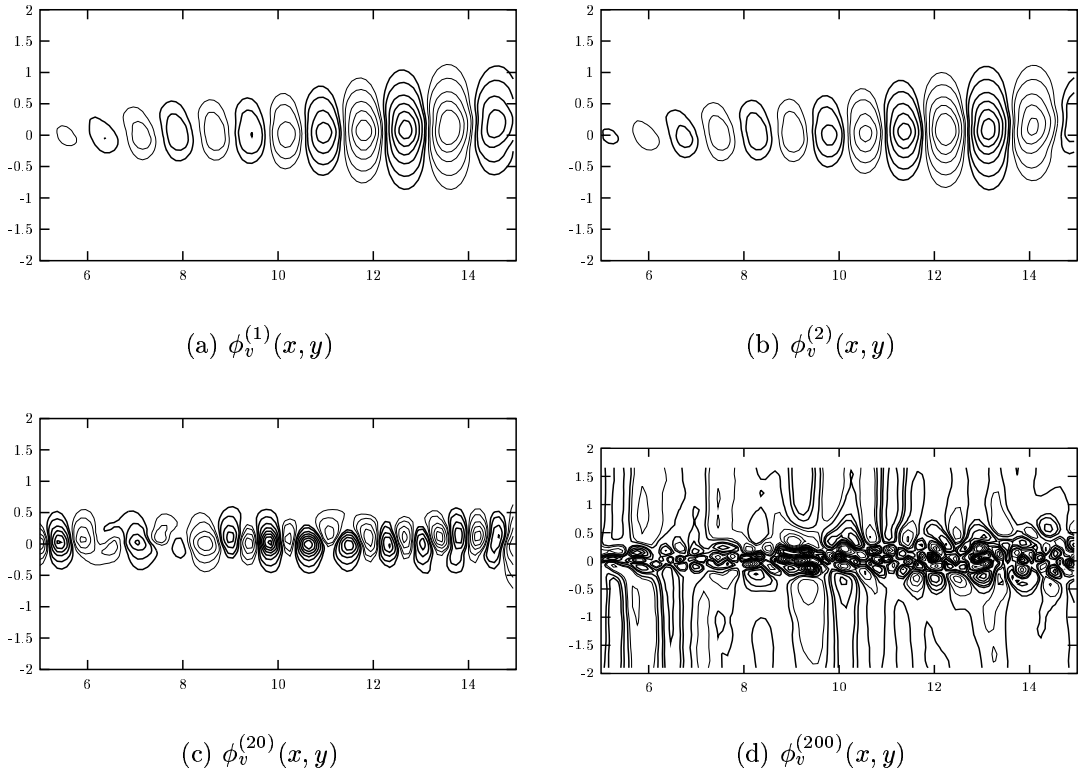

(a) $\phi_v^{(1)}(x,y)$ (b) $\phi_v^{(2)}(x,y)$

(c) $\phi_v^{(20)}(x,y)$ (d) $\phi_v^{(200)}(x,y)$

Figure 5: Iso-contours of the spatial eigenfunctions $\phi_v^{(n)}(x,y)$ obtained from the scalar-POD applied to the velocity component v ($n = 1, 2, 20$ and 200).

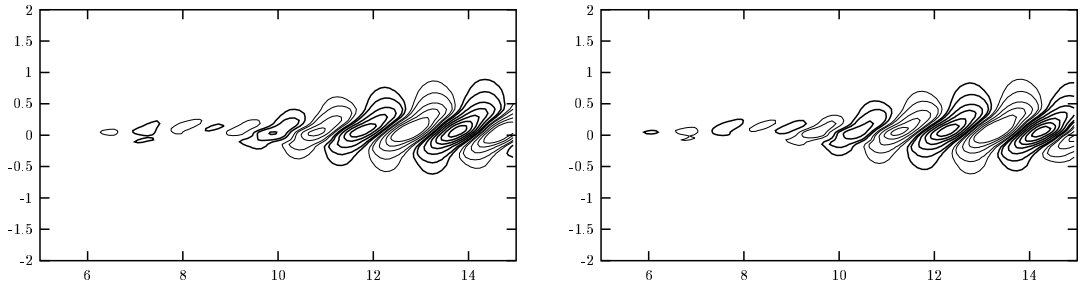

(a) $\phi_w^{(1)}(x,y)$ (b) $\phi_w^{(2)}(x,y)$

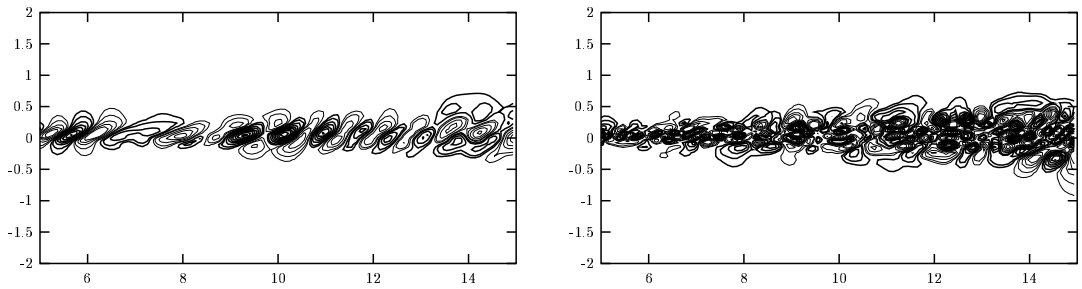

(c) $\phi_w^{(20)}(x,y)$ (d) $\phi_w^{(200)}(x,y)$

Figure 6: Iso-contours of the spatial eigenfunctions $\phi_w^{(n)}(x,y)$ obtained from the scalar-POD applied to the velocity component w ($n = 1, 2, 20$ and 200).

ticed for the spatial eigenfunctions (see §3.2.2). Since the same phenomenon is observed for the temporal eigenfunctions of the snapshot POD applied to the stationary cylinder flow (see figure 21), it was explained in §8.3.2.

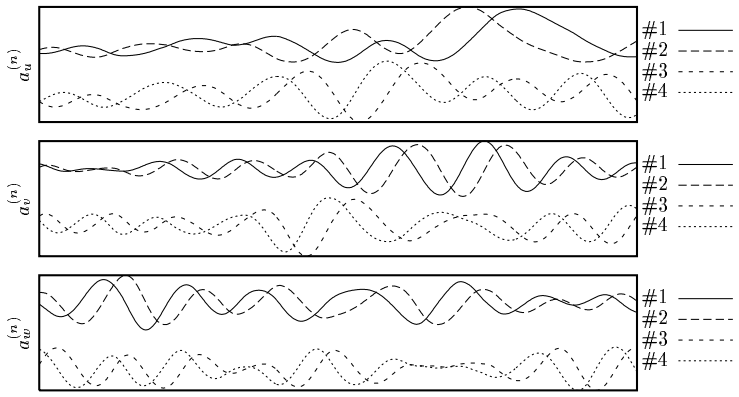

Figure 7: Temporal evolution of the expansion coefficients $a_i^{(n)}(z,t)$ deduced from the scalar-PODS of the u, v and w component of the velocity.

3.2.4 Scalar-PODs validations

The good agreement between the computations and the experiments (see §2.2) can also be exhibited when the two-point space correlations $R_{ii}(x_0, y_0, x', y')$ are considered. By application of the Mercer's theorem (see Cordier and Bergmann, 2002, equation (26), §4.2), this correlation can be estimated from the results of the scalar-PODs as:

$$R_{ii}(x_0, y_0, x', y') = \sum_{n=1}^{200} \lambda^{(n)} \phi_i^{(n)}(x_0, y_0) \phi_i^{(n)}(x', y') \tag{10}$$

In order to cross-validate computations and experiments, the space-time correlations experimentally determined by Delville (1995) through Taylor hypothesis is compared in figure 8 to the contribution of the first 200 POD modes estimated with equation (10). On this figure, the reference point (x_0, y_0) is located at the center of the selected spatial domain. Very good agreements are achieved. We must underline that the overall shape of the measured correlations is also well described by considering only few first POD modes. Note that the u component can be described by fluctuations of opposite sign from part to part of the mixing layer, while the v component can be described by fluctuations in phase all over the y direction, alternated in sign in the x direction. Moreover, the shape of the w component indicates

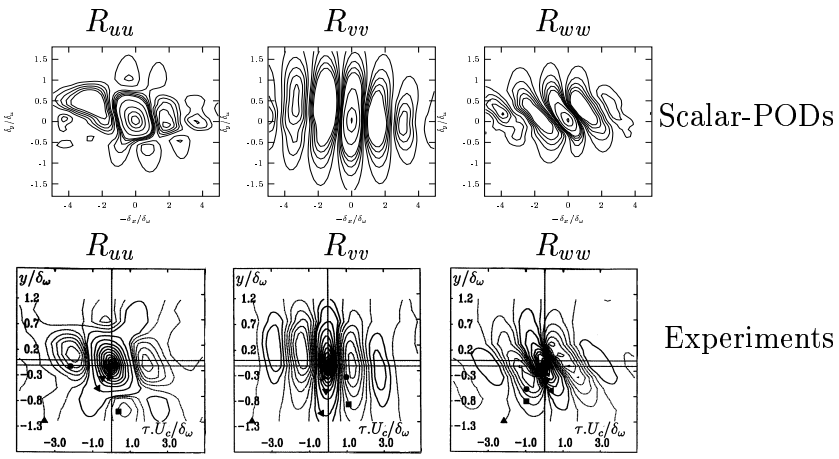

Figure 8: Comparison in a plane (τ, y) or $(-x, y)$ of the experimentally measured space time correlations $R_{ii}(\tau; y, y')$ (bottom) with the space correlations obtained from the contribution of the first 200 modes of the scalar PODs (top).

the presence of a strong organization for the streamwise vorticity component, this organization being recovered from both experiments and LES.

4 Coherent structures of the plane mixing layer

4.1 Description of the snapshot POD

In order to analyze the spatial organization present in the mixing layer, the snapshot POD method (see Cordier and Bergmann, 2002, §5.4) is applied on the numerical results obtained by LES. As it was explained in §5.6 of Cordier and Bergmann (2002), since numerical simulations are highly resolved in space but suffer from rather limited temporal samples compared to experiments, the snapshot POD is preferred to the classical POD.

To make these lecture notes self-contained, we sketch in the following the main lines[7] of the snapshot POD method.

First, we decompose every spatio-temporal event $v_i(\vec{\boldsymbol{x}}, t)$ as a mean and

[7]Except for the notations, this description of the snapshot POD is similar to the contents of §8.3.1 where an algorithm describing the computation of POD basis functions for the cylinder flow is presented.

a fluctuating parts:

$$v_i(\vec{\boldsymbol{x}},t) = \overline{v_i}(\vec{\boldsymbol{x}}) + v_i'(\vec{\boldsymbol{x}},t) \tag{11}$$

where the mean part is expressed with an average in time:

$$\overline{v_i}(\vec{\boldsymbol{x}}) = \frac{1}{T}\int_T v_i(\vec{\boldsymbol{x}},t)\,dt$$

The fluctuating quantities can be written using a discrete basis of the flow:

$$v_i(\vec{\boldsymbol{x}},t) = \sum_{n=1}^{N_{POD}} A^{(n)}(t)\ \Phi_i^{(n)}(\vec{\boldsymbol{x}}) \tag{12}$$

where N_{POD} is the number of modes solved in the POD.

The temporal eigenfunctions $A^{(n)}(t)$ are then calculated by means of a Fredholm integral equation:

$$\int_T C(t,t')\ A^{(n)}(t')\ dt' = \Lambda^{(n)}\ A^{(n)}(t) \tag{13}$$

where $C(t,t')$ is the temporal velocity correlations:

$$C(t,t') = \frac{1}{T}\int_\Omega v_i'(\vec{\boldsymbol{x}},t)\ v_i'(\vec{\boldsymbol{x}},t')\ d\vec{\boldsymbol{x}} = \frac{1}{T}\sum_{n=1}^{N_{POD}} A^{(n)}(t)\ A^{(n)}(t') \tag{14}$$

and where $\Lambda^{(n)}$ are the (real, positive) eigenvalues of this tensor. Each eigenvalue is associated to the energy density contained in the corresponding mode and the sum of $\Lambda^{(n)}$ is equal to the turbulent kinetic energy included in the integral domain Ω.

The spatial eigenfunctions are then deduced from:

$$\Phi_i^{(n)}(\vec{\boldsymbol{x}}) = \frac{1}{T\Lambda^{(n)}}\int_T v_i(\vec{\boldsymbol{x}},t)\ A^{(n)}(t)\ dt \tag{15}$$

where they verified the orthogonality condition:

$$\int_\Omega \Phi_i^{(n)}(\vec{\boldsymbol{x}})\ \Phi_i^{(m)}(\vec{\boldsymbol{x}})\ d\vec{\boldsymbol{x}} = \delta_{mn}\ . \tag{16}$$

4.2 Application of the snapshot POD

The snapshot POD method is applied on the filtered velocity field provided by projecting the flow realizations obtained by the LES on the first N^{KL} modes of the scalar-PODs (see §3). The temporal correlations $C(t,t')$ are then estimated on 1000 time steps and over a limited portion of the computational domain ($x/\delta_{\omega_0} \in [5;15]$).

4.2.1 Snapshot POD convergence

The relative information content of the snapshot POD is plotted on figure 9. The convergence is also very rapid since 99 % of the turbulent kinetic energy is contained within the 64 first modes. However, while the Karhunen-Loève dimension seems lower in the snapshot POD, the relative number of modes required to contain 99% of energy (N^{KL}/N_{POD}=0.064) remains of the same order of magnitude than in the scalar POD cases (N^{KL}/N_{POD}=0.1).

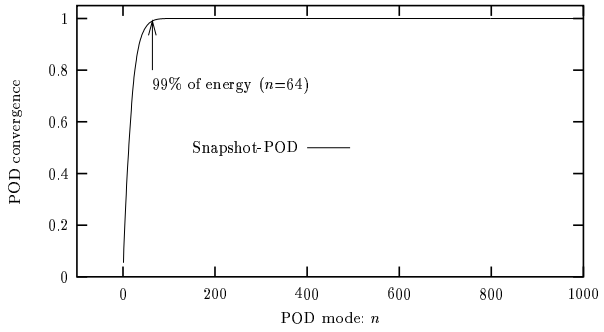

Figure 9: Relative information content for the snapshot POD.

If we represent the eigenvalue spectrum of the Fredholm equation (13), it is notable that these eigenvalues occur in pair of almost equal values, whereas there is a gap in magnitude between these pairs. The eigenvalue problem is near degenerate. This characteristic is encountered in many POD applications and it is further discussed in §8.3.2 where the snapshot POD is applied to the cylinder flow.

4.2.2 Spatial eigenfunctions

The spatial eigenfunctions $\Phi_i^{(n)}(\vec{\boldsymbol{x}})$ are then deduced from the temporal eigenfunctions $A^{(n)}(t)$ by means of equation (15). In figure 10 are plotted positive iso-surfaces of the spatial eigenfunctions for the two first POD modes. The same features as already noticed in the scalar-PODs (see figures 4, 5 and 6) are observed. Mainly, whatever the velocity components are, a streamwise shift is noticed when comparing mode 1 and mode 2. This behaviour is also found for the cylinder flow and the reader is referred to §8.3.2 for a complete discussion of this phenomenon. Moreover, these eigenfunctions exhibit a preferred organization in the spanwise direction. Particularly, $\Phi_v^{(n)}(\vec{\boldsymbol{x}})$ is clearly aligned in the spanwise direction and $\Phi_w^{(n)}(\vec{\boldsymbol{x}})$ exhibits lambda-shape like structures (see figure 10). These behaviours are similar to those observed in the analysis of the experimental data by Delville (1995).

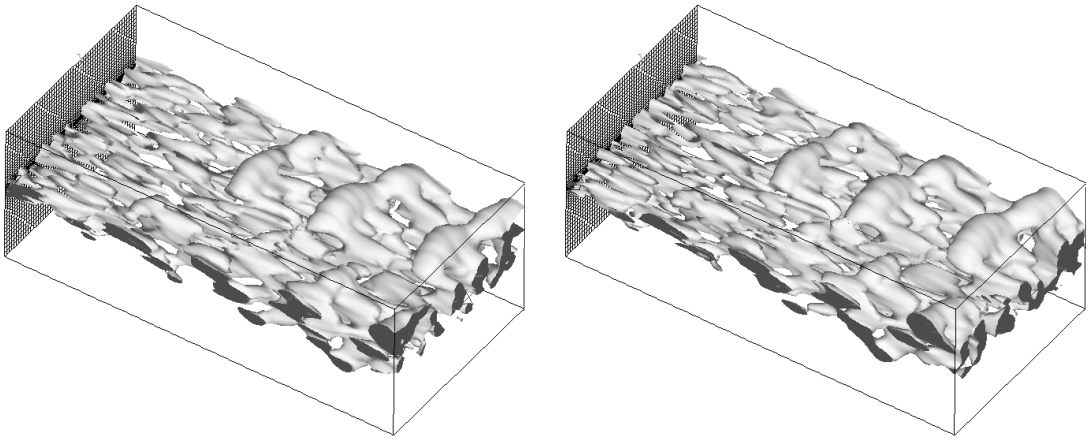

(a) $\Phi_u^{(1)}(\vec{x})$ (b) $\Phi_u^{(2)}(\vec{x})$

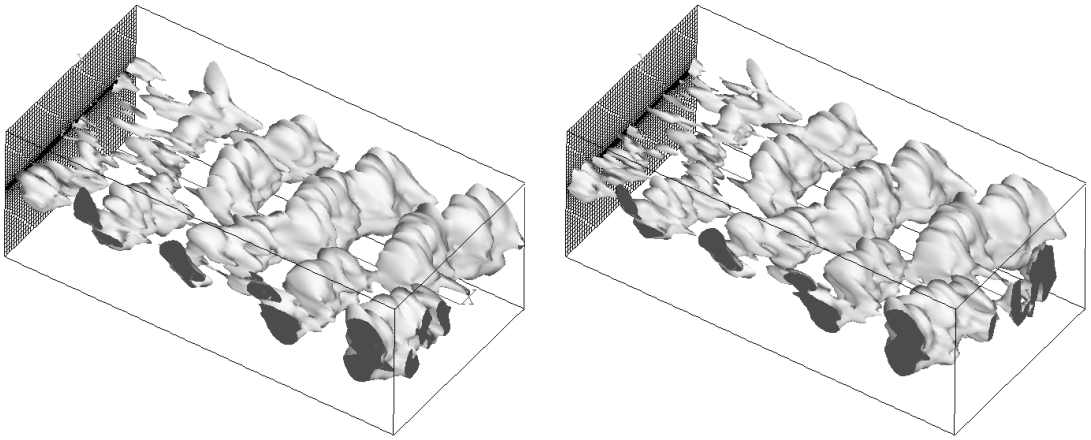

(c) $\Phi_v^{(1)}(\vec{x})$ (d) $\Phi_v^{(2)}(\vec{x})$

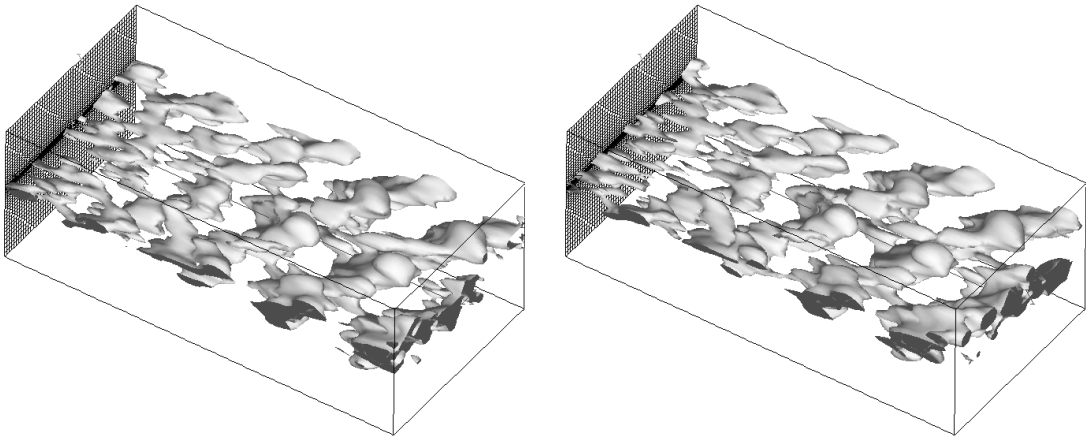

(e) $\Phi_w^{(1)}(\vec{x})$ (f) $\Phi_w^{(2)}(\vec{x})$

Figure 10: Iso-surface of the spatial eigenfunctions of the snapshot POD for the three components of velocity. Mode 1 (left), mode 2 (right).

To sum up the results of this study, the spatial eigenfunctions $\phi_i^{(n)}(x,y)$ determined via the scalar-PODs mimic very well the coherent structures organization since a good agreement is achieved between their contribution to the space correlations and the correlations experimentally obtained (see §3.2.4). Using the compressed data, a three-dimensional snapshot POD has been performed. The spatial organization of the eigenfunctions $\Phi_i^{(n)}(x,y,z)$ can be favorably compared to the experimental ones.

Finally, in Cordier*et al.* (1997), a low-order dynamical system has been derived from the snapshot POD eigenfunctions to study the temporal evolution of these large scale coherent structures. This point is not developed here but a similar treatment can be found in §8.4 for the cylinder flow.

5 Acknowledgements

The study presented in this part of the lectures notes has been performed during a one year postdoctoral position held by one of the authors (LC) at the Laboratoire d'Etudes Aérodynamiques (France). LC gratefully acknowledges Joël Delville (LEA) and Christian Tenaud (LIMSI, France) for their help during the process of this work. The LES numerical code as described in §2.1 was written by Dr R. Lardat (LIMSI). Drs Tenaud and Ta Phuoc (LIMSI) are greatly acknowledged for their numerous and valuable comments and discussions on the numerics. The calculations have been performed on the Cray C90 of the Institut du Développement et des Ressources en Informatique Scientifique (IDRIS / CNRS) Orsay, France. LC is also grateful to these institutions for their support.

Part II
Reduced Order Modelling (ROM) based on POD

6 Introduction

6.1 Motivations

The main objective of this part is to investigate computational methods based on POD for the optimal control[8] of incompressible viscous flow. Flow control has a long history since Prandtl's early experiments for delaying boundary layer separation (see Prandtl, 1925). However, the recent invention of Micro-ElectroMechanical Systems (see Gad-el-Hak, 2002, for an introduction of MEMS) has generated a renewal of interest in active control of fluid dynamical systems (see Gunzburger, 1995; Gad-el-Hak, 2000, for a comprehensive survey).

In a flow control or optimization setting, the large-scale systems obtained by spatial discretization of the governing equations need to be solved repeatedly and this represents the dominant part of the computational costs. Therefore, there is a demand to use reduced order models that serve as low-dimensional approximation models to the large-scale discretized state equations. There are a number of choices (see Ito and Ravindran, 1998, for a presentation) for reduced bases: Lagrange basis, Hermite basis, Taylor basis, POD basis, ... Here, we decide to model the non-linear dynamics of the flow via a reduced order model based on POD functions.

In Cordier and Bergmann (2002), it was shown that the POD eigenfunctions form a complete set of orthonormal functions i.e. each space-time realization $\vec{\boldsymbol{u}}(\vec{\boldsymbol{x}},t)$ can be expanded in eigenfunctions as:

$$\vec{\boldsymbol{u}}(\boldsymbol{x},t) = \sum_{m=1}^{N_{POD}} a^{(m)}(t)\vec{\boldsymbol{\Phi}}^{(m)}(\vec{\boldsymbol{x}}) \tag{17}$$

[8]Recently, interest has increased to use POD methods for optimal flow control of viscous fluids. The optimization problems of fluid flow are among the most challenging in computational science and engineering, explaining the reason for the choice of this application to illustrate POD. However, the reader must note that other typical applications of POD, like low-cost simulations or study of the dynamics of turbulent flows (see Aubry *et al.*, 1988; Ukeiley *et al.*, 2001), share the same key features. Therefore, the reader who is not directly interested to flow control problem will find nevertheless in the following sections important results necessary to derive a POD reduced order model.

with

$$a^{(n)}(t) = \left(\vec{\boldsymbol{u}}(\boldsymbol{x},t), \vec{\boldsymbol{\Phi}}^{(n)}(\vec{\boldsymbol{x}})\right) = \int_{\Omega} \vec{\boldsymbol{u}}(\boldsymbol{x},t) \cdot \vec{\boldsymbol{\Phi}}^{(n)*}(\vec{\boldsymbol{x}})\, d\vec{\boldsymbol{x}}, \tag{18}$$

where $\vec{\boldsymbol{\Phi}}^{(m)}(\vec{\boldsymbol{x}})$ are the spatial POD eigenfunctions and N_{POD} is the number of POD modes. Here, our objective is to use the energetic optimality of convergence of the POD basis functions for deriving low-dimensional dynamical models for the expansion coefficients $a^{(n)}(t)$ of equation (17). A common procedure for obtaining such equations is the method of Galerkin Projection described extensively in §7. Given an ensemble data obtained for a specific flow configuration, e.g., for an uncontrolled flow, the Galerkin procedure leads to a reduced order model for the Navier-Stokes equations, such that it is a suitable model for representing the corresponding flow dynamics. However, if you are interested to apply the reduced order modelling idea to flow control, there is no guarantee that the previously derived reduced order model can provide useful approximations to flow dynamics altered by control. This fundamental question is discussed with more details in the next section.

6.2 Use of approximation models for optimization

Until recently, it was commonly assumed that effective reduced order models for predictive control can be constructed from the POD basis of an uncontrolled flow. The possible modifications of the POD basis functions under the action of control were neglected. The general approach was to approximate the equations of the fluid flow by POD reduced order models and then to apply an exact optimization procedure for the reduced systems (see Ravindran, 2000b, for example). The conceptual drawback is that there is no mathematical assurance that the solution of the optimization algorithm working with the approximation models will correspond to the solution of the optimization problem for the original dynamical system. In a recent study, Prabhu *et al.* (2001) address this question and demonstrate for wall-bounded turbulent flows that a no-control basis used as a low-dimensional model will not capture the key features of these controlled flows. Consequently, some sort of iterative technique is required, in which the construction of reduced order models is coupled with the progresssion of the optimization process.

Figure 11 from Alexandrov *et al.* (1997) describes how to use approximation models in the context of optimization. The basic idea is to use occasionally information from the high-fidelity model to check design parameters generated using a model of lower fidelity but of lower computational cost. This simpler but cheaper approximation model is used to take a number of

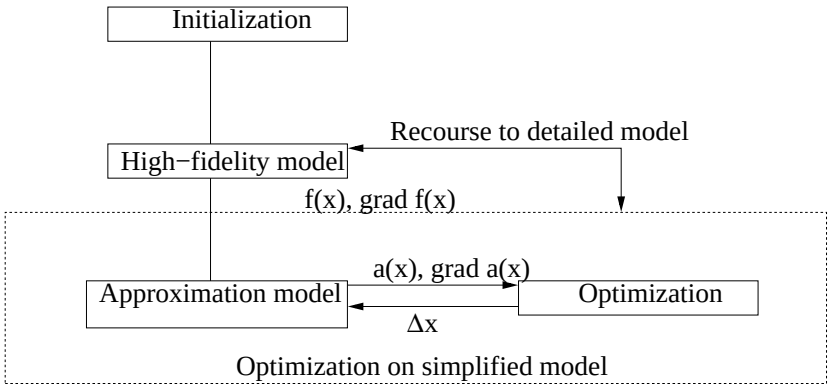

Figure 11: Optimization algorithm using approximation models.

optimization iterations. At the end of this optimization phase, one has recourse to the high fidelity model to recalibrate the lower-fidelity model before to continue the optimization process with the simplified model. Ravindran (2000a) introduced such an adaptative procedure and improved the reduced order model by successively updating the input collection. The snapshots corresponding to a specified control input (not necessarily optimal) are first computed. With these snapshots, a POD subspace is found and the corresponding reduced order control system derived. The optimal control problem is then solved and the resulting control is applied to the Navier-Stokes equations to generate a new input data. With this new ensemble, another POD basis is determined, a new reduced order control system derived and a new optimal control computed. Finally, this process is stopped when the convergence is achieved i.e. when the variation in absolute value of the control input between two successive iterations is less than a given small parameter. Despite this fairly crude criterion, Ravindran presents numerical results that seem to indicate that his adaptive procedure is quite effective for a recirculation control problem. In order to make such an iterative scheme robust (i.e. to be assured that the solution of the optimization problem for the reduced order model is likely to yield at least to a local optimum for the original, high fidelity problem), Alexandrov *et al.* (1997) proposed to use the general trust region framework[9] (see Conn *et al.*, 2000, for a comprehensive survey of the trust region methods). The trust region mechanism gives a measure of how well the approximation model is predicting improvement in the high-fidelity model and thus suggests criteria for automatically changing or improving the

[9]This philosophy of combining trust-region methods with general modelling issues is a well-known technique in multidisciplinary design optimization also known as surrogate optimization (see Booker *et al.*, 1998; Alexandrov *et al.*, 1999).

reduced model when poor or incorrect prediction of improvement is obtained. For further informations, the reader is referred to Fahl (2000) who presents an algorithm that implements the combination of POD based reduced order modelling and trust region methods, the TRPOD (Trust Region Proper Orthogonal Decomposition).

In this part, an example of the development of a POD reduced order model is presented in §8 for the incompressible unsteady wake flow behind a circular cylinder. After a description of the flow numerical simulation in §8.2, the snapshot POD is applied to data corresponding to the stationary cylinder flow (see §8.3). Afterward, a reduced order model is derived for the stationary flow in §8.4 by Galerkin Projection of the governing equations into the POD subspace. In the same section, numerical evidence is presented that a six mode model provides a satisfactory description of the long term dynamics of the flow. Finally, in §8.5, we present a method introduced by Graham *et al.* (1999a) and called *control function method* that can be used to incorporate into the low-order dynamical system, the motion of the control surface. Since this lecture series is dedicated to post-processing of data and not to active flow control, no numerical results is presented for the controlled flow. Use of the TRPOD method for controlling the cylinder flow is in progress and results will be published elsewhere.

7 Galerkin Projection (GP)

7.1 General methodology

Before going into the details of the application of the Galerkin Projection for the POD eigenfunctions (see §7.2), we first recall the basic ideas of GP.

Galerkin Projection is a special case of *weighted residual methods* (see Fletcher, 1991). These methods are dedicated to solve functional equations, like ordinary or partial differential equations, or integral equations. For example, consider the equation

$$\mathcal{L}(\vec{u}) = 0 \tag{19}$$

defined in a domain Ω where $\mathcal{L}$ is some differential operator. The Galerkin method is an approximation to the true solution of (19) sought by weighting the residual of the differential equation. Assume $\vec{U}$ is an approximate solution to (19). Substitution of $\vec{U}$ for $\vec{u}$ in (19) results in a non-zero residual $r = \mathcal{L}(\vec{U}) \neq 0$.

The best approximation for $\vec{\boldsymbol{U}}$ is that which reduces the residual r to the least value at all points in the domain Ω. The weighted residual method enforces the condition

$$R_j = \int_\Omega w_j \, r \, d\Omega = 0 \tag{20}$$

where R_j are the weighted residual integrals and w_j are the weighting functions. In the Galerkin method, the weighting functions are chosen to be the same as the basis functions used in the expansion of the approximate solution. Hence, if $\vec{\boldsymbol{U}}$ is approximated by the expansion

$$\vec{\boldsymbol{U}}(\vec{\boldsymbol{x}}) = \sum_{i=1}^{\infty} \chi_i \vec{\boldsymbol{\varphi}}_{\boldsymbol{i}}(\vec{\boldsymbol{x}}) \tag{21}$$

where $\vec{\boldsymbol{\varphi}}_{\boldsymbol{i}}(\vec{\boldsymbol{x}})$ are the basis functions and χ_i are the coefficients to be determined, then the weighting functions are selected as $w_j = \vec{\boldsymbol{\varphi}}_{\boldsymbol{j}}(\vec{\boldsymbol{x}})$, $j = 1, \cdots, +\infty$. The fact that the unknown $\vec{\boldsymbol{u}}$ solution of (19) is a member of an infinite dimensional space is a practical difficulty. The discretization step of the Galerkin procedure then consists ot truncating the sum in (21) at a finite index i_{max}, thus rendering the problem a finite dimensional one. Therefore, (20) becomes:

$$\int_\Omega \vec{\boldsymbol{\varphi}}_{\boldsymbol{j}}(\vec{\boldsymbol{x}}) \, \mathcal{L}(\vec{\boldsymbol{U}}) \, d\Omega = 0 \qquad j = 1, \cdots, i_{max} \tag{22}$$

If the definition (18) of the inner product is introduced, then equation (22) further simplifies to

$$\left(\mathcal{L}(\sum_{i=1}^{i_{max}} \chi_i \vec{\boldsymbol{\varphi}}_{\boldsymbol{i}}(\vec{\boldsymbol{x}})), \vec{\boldsymbol{\varphi}}_{\boldsymbol{j}} \right) = 0 \qquad j = 1, \cdots, i_{max} \tag{23}$$

Finally, the Galerkin Projection is equivalent to impose the i_{max} scalar products defined by equation (23) to vanish.

For such an approach to work (see Rempfer, 1996), the two following requirements should be satisfied:

1. the function space $\{\vec{\boldsymbol{\varphi}}_{\boldsymbol{i}}\}$ of the basis functions $\vec{\boldsymbol{\varphi}}_{\boldsymbol{i}}(\vec{\boldsymbol{x}})$ must be complete and for practical reasons to become clear in §7.2, an orthonormal basis is especially desirable.

2. the basis functions $\vec{\boldsymbol{\varphi}}_{\boldsymbol{i}}(\vec{\boldsymbol{x}})$ must meet the boundary conditions of the problem.

7.2 POD based Reduced Order Models

From the properties of the POD eigenfunctions $\vec{\Phi}^{m}(\vec{x})$ as described in §4.2 of Cordier and Bergmann (2002) one can immediately see that these eigenfunctions are particularly suited for Galerkin Projection.

The Navier-Stokes equations for incompressible flows can be written symbolically as:

$$\frac{\partial \vec{u}}{\partial t} = \vec{F}(\vec{u}) \quad \text{with } \vec{u} = \vec{u}(\vec{x}, t) \;\; \vec{x} \in \Omega \;\text{ and }\; t \geq 0 \tag{24}$$

where $\vec{F}$ is a differential operator that contains only spatial derivatives and where Ω is the spatial domain under study. The differential equation (24) is mathematically well posed if the system is completed by initial conditions:

$$\vec{u}(\vec{x}, t = 0) = \vec{u_0}(\vec{x}) \tag{25}$$

and boundary conditions. Here, we decide to follow the viewpoint of Fahl (2000) and to formulate the differential equation (24) in the general context of boundary control problem for fluid flows. Hence, we assume that the boundary of the domain Γ, can be split into two parts such that Γ_c denotes that part of the boundary where the control is applied and $\Gamma \setminus \Gamma_c$ is the part of the boundary that is not controlled. Then, we can complete the equations (24) with the Dirichlet boundary conditions:

$$\vec{u}(\vec{x}, t) = \vec{h}(\vec{x}, t; d(t)) \quad \text{with} \quad \vec{x} \in \Gamma \;\text{ and }\; t \geq 0 \tag{26}$$

where d is the control input. More precisely, the boundary conditions can be written as:

$$\vec{h}(\vec{x}, t; d(t)) = \begin{cases} \gamma(t)\vec{c}(\vec{x}) & \vec{x} \in \Gamma_c,\ t \geq 0, \\ \vec{g}(\vec{x}) & \vec{x} \in \Gamma \setminus \Gamma_c,\ t \geq 0, \end{cases} \tag{27}$$

where $\gamma(t)$ can be interpreted as the temporal variation of a prescribed control action defined by $\vec{c}(\vec{x})$, $\vec{x} \in \Gamma_c$. For example, this formulation corresponds to flow control by blowing and suction along a portion of the boundary as considered in Joslin *et al.* (1995).

The reduced order model is then derived by Galerkin Projection of the partial differential equation (24) onto the POD subspace of dimension N_{POD}. The first step is to insert in (24) the development of $\vec{u}$ on the POD basis $\vec{\Phi}^{(m)}$:

$$\vec{u}(\boldsymbol{x}, t) = \sum_{m=1}^{N_{POD}} a^{(m)}(t)\vec{\Phi}^{(m)}(\vec{x}) \tag{28}$$

to obtain:

$$\sum_{m=1}^{N_{POD}} \frac{da^{(m)}(t)}{dt}\vec{\mathbf{\Phi}}^{(m)}(\vec{\boldsymbol{x}}) = \vec{\boldsymbol{F}}\Big(\sum_{m=1}^{N_{POD}} a^{(m)}(t)\vec{\mathbf{\Phi}}^{(m)}(\vec{\boldsymbol{x}})\Big) \tag{29}$$

The set of spatial eigenfunctions $\vec{\mathbf{\Phi}}^{(m)}(\vec{\boldsymbol{x}})$ being a basis, the right-hand side of (29) can be written as a linear combination of the $\vec{\mathbf{\Phi}}$:

$$\vec{\boldsymbol{F}}\Big(\sum_{m=1}^{N_{POD}} a^{(m)}(t)\vec{\mathbf{\Phi}}^{(m)}(\vec{\boldsymbol{x}})\Big) = \sum_{n} \mathcal{F}^{(n)}\left(a^{(1)}, a^{(2)}, \cdots\right)\vec{\mathbf{\Phi}}^{(n)}(\vec{\boldsymbol{x}}) \tag{30}$$

Finally, the Galerkin Projection of (24) onto the POD eigenfunctions is evaluated as:

$$\left(\vec{\mathbf{\Phi}}^{(n)}, \frac{\partial\vec{\boldsymbol{u}}}{\partial t}\right) = \left(\vec{\mathbf{\Phi}}^{(n)}, \vec{\boldsymbol{F}}(\vec{\boldsymbol{u}})\right) \qquad \text{for } n = 1, \cdots, N_{gal} \tag{31}$$

where N_{gal} is the number of Galerkin modes kept in the projection.

From the orthonormality[10] of the eigenfunctions $\vec{\mathbf{\Phi}}^{(m)}(\vec{\boldsymbol{x}})$, the Partial Differential Equation (24) is replaced by a set of Ordinary Differential Equations defined as:

$$\frac{da^{(n)}(t)}{dt} = \mathcal{F}^{(n)}\big(a^{(1)}(t), \cdots, a^{(n)}(t)\big) \text{ with } n = 1, \cdots, N_{gal} \tag{32}$$

where

$$\mathcal{F}^{(n)} = \left(\vec{\mathbf{\Phi}}^{(n)}, \vec{\boldsymbol{F}}\Big(\sum_{m=1}^{N_{gal}} a^{(m)}(t)\vec{\mathbf{\Phi}}^{(m)}(\vec{\boldsymbol{x}})\Big)\right). \tag{33}$$

The functions $\mathcal{F}^{(n)}$ are linear if $\vec{\boldsymbol{F}}$ is a linear operator and, in our case, due to the convective terms in the Navier-Stokes equations, $\mathcal{F}^{(n)}$ are usually quadratic functions of $a^{(n)}$. In Aubry *et al.* (1988) and Ukeiley *et al.* (2001), the low-order dynamical system (32) have cubic terms because the velocity field is decomposed into mean and fluctuating components ($\vec{\boldsymbol{u}} = \langle\vec{\boldsymbol{u}}\rangle + \vec{\boldsymbol{u}'}$), where the mean is slowly varying in time. The mean may then be described

[10] The left-hand side of (32) is estimated as

$$\left(\vec{\mathbf{\Phi}}^{(n)}, \sum_{m=1}^{N_{gal}} \frac{da^{(m)}(t)}{dt}\vec{\mathbf{\Phi}}^{(m)}(\vec{\boldsymbol{x}})\right) = \sum_{m=1}^{N_{gal}} \frac{da^{(m)}(t)}{dt}\left(\vec{\mathbf{\Phi}}^{(n)}, \vec{\mathbf{\Phi}}^{(m)}\right).$$

Hence, as previously noted in §7.1, an orthonormal basis is especially desirable because we avoid inverting an $N_{gal} \times N_{gal}$ matrix to solve for $\dot{a}^{(n)}(t)$.

in terms of the fluctuations $\vec{\boldsymbol{u}}'$, which give rise to Reynolds stresses and then to cubic equations for (32). Another enhancement to the basic theory described so far is the modeling of energy transfer to the higher modes[11] neglected in the Galerkin Projection procedure. In Aubry *et al.* (1988), the influence of the missing scales is simply parameterized by a generalization of the Heisenberg spectral model in homogeneous turbulence (see Hinze, 1975) and in Ukeiley *et al.* (2001) the mean velocity is split into a steady and time-dependent part by choosing cutoff wavenumbers.

To obtain a well-posed mathematical problem, one needs to add a set of initial conditions to the reduced order model (32) and to make sure that the problem (32) matches the original boundary conditions (26).

The initial conditions can be directly inferred from the conditions (25) imposed to the original problem:

$$a^{(n)}(t=0) = a_0^{(n)} \quad \text{where} \quad a_0^{(n)} = \left(\vec{\boldsymbol{u}}_{\mathbf{0}}(\vec{\boldsymbol{x}}), \vec{\boldsymbol{\Phi}}^{(\boldsymbol{n})}\right) \tag{34}$$

For the boundary conditions, the answer is not so direct because it depends mainly of the type of boundary conditions applied, homogeneous or nonhomogeneous boundary conditions. For this reason, this question is postponed to §7.3.

To sum up, combining the Galerkin Projection (§7.1) and the optimality of convergence of POD eigenfunctions (see Cordier and Bergmann, 2002, §4.3), we demonstrate that high-dimensional models represented by Partial Differential Equations (PDE) can be replaced by low-dimensional dynamical models of non linear Ordinary Differential Equations (ODE).

7.3 The problem of boundary conditions

In §5.5.2 of Cordier and Bergmann (2002), it was demonstrated that the POD eigenfunctions $\vec{\boldsymbol{\Phi}}^{(n)}$ can be represented as linear combinations of instantaneous velocity fields:

$$\vec{\boldsymbol{\Phi}}^{(n)}(\boldsymbol{x}) = \frac{1}{T\,\lambda^{(n)}} \int_T \vec{\boldsymbol{u}}(\boldsymbol{x},t) a^{(n)*}(t)\; dt \tag{35}$$

where $\lambda^{(n)}$ are the POD eigenvalues and T the period of time during which the input data are collected.

[11] These higher modes correspond to the dissipative scales of the flow.

According to (35), when the Navier-Stokes Equations (NSE) are subjected to homogeneous Dirichlet boundary conditions (for example $\vec{\boldsymbol{h}}(\vec{\boldsymbol{x}}, t; c(t)) = \vec{\mathbf{0}}$), the POD basis functions inherit these boundary conditions. Therefore, the reduced order models developed by Galerkin Projection of the NSE on the POD subspace are equivalent[12] to the original NSE. The expansion coefficients $a_{DS}^{(n)}(t)$, $n = 1, \cdots, N_{gal}$ solutions of the dynamical system (32) can then be used to compute the reduced order solution

$$\vec{\boldsymbol{u}}_{DS}(\boldsymbol{x}, t) = \sum_{m=1}^{N_{gal}} a_{DS}^{(m)}(t) \vec{\boldsymbol{\Phi}}^{(m)}(\vec{\boldsymbol{x}}) \tag{36}$$

where the subscript DS denotes the dynamical system approximation to the original solution $\vec{\boldsymbol{u}}(\boldsymbol{x}, t)$ of the NSE.

Now we consider the NSE with non homogeneous Dirichlet boundary conditions defined by (27). Assume that the snapshots data $\vec{\boldsymbol{u}}(\vec{\boldsymbol{x}}, t_i)$, $i = 1, \cdots, N_t$ of the input ensemble $\mathcal{U}$ verify the required (non homogeneous) boundary conditions. Due to (35), the POD basis functions are no longer suitable to use in a Galerkin Projection. The solution of this problem is to transform the actual problem to a problem with homogeneous boundary conditions.

When $\vec{\boldsymbol{h}}(\vec{\boldsymbol{x}}, t; d(t))$ does not depend on time t, for example $\vec{\boldsymbol{h}}(\vec{\boldsymbol{x}}, t; d(t)) = \vec{\boldsymbol{g}}(\vec{\boldsymbol{x}})$ for all $\vec{\boldsymbol{x}} \in \Gamma$ and $t \geq 0$, Sirovich (1987a) suggests to overcome this difficulty by computing the POD basis functions for the fluctuations around the mean flow field. Given N_t time snapshots, the mean velocity $\langle \vec{\boldsymbol{u}}(\vec{\boldsymbol{x}}, t) \rangle = \frac{1}{N_t} \sum_{i=1}^{N_t} \vec{\boldsymbol{u}}(\vec{\boldsymbol{x}}, t_i)$ is first computed as an ensemble average. The POD eigenfunctions are then estimated using the modified input data $\mathcal{U}' = \{\vec{\boldsymbol{u}}(\vec{\boldsymbol{x}}, t_1) - \langle \vec{\boldsymbol{u}}(\vec{\boldsymbol{x}}, t) \rangle, \cdots, \vec{\boldsymbol{u}}(\vec{\boldsymbol{x}}, t_{N_t}) - \langle \vec{\boldsymbol{u}}(\vec{\boldsymbol{x}}, t) \rangle\}$ (see §8.3 for an example). Due to its construction, the mean flow $\langle \vec{\boldsymbol{u}}(\vec{\boldsymbol{x}}, t) \rangle$ is a solenoidal field and satisfies the prescribed non homogeneous boundary conditions. Furthermore, each modified snapshot $\vec{\boldsymbol{u}}(\vec{\boldsymbol{x}}, t_i) - \langle \vec{\boldsymbol{u}}(\vec{\boldsymbol{x}}, t) \rangle$ is also divergence free, but satisfies homogeneous Dirichlet boundary conditions. In the case of time-independent

[12] More precisely, we can only argue that the system of ODEs (32) are mathematically equivalent to the original problem (24). We are sure that there exists a solution of the reduced order model (32) that lies on the manifold that is defined by the boundary conditions of the original problem. However, the fundamental question to know if a flow can be represented exactly by a finite-dimensional basis of POD eigenfunctions and the question of stability of that manifold are still not fully answered. Issues concerning the stability and the accuracy of a Galerkin Projection are discussed in Iollo (1997) and Iollo *et al.* (1998). The possible connections between the stability properties of the manifold and the stability properties of the physical phenomenon are addressed in Rempfer (1996).

non homogeneous boundary conditions, the reduced order solution can be computed as:

$$\vec{\boldsymbol{u}}_{DS}(\boldsymbol{x},t) = \langle \vec{\boldsymbol{u}}(\vec{\boldsymbol{x}},t)\rangle + \sum_{m=1}^{N_{gal}} a_{DS}^{(m)}(t)\vec{\boldsymbol{\Phi}}^{(m)}(\vec{\boldsymbol{x}}) \tag{37}$$

where the coefficients $a_{DS}^{(n)}(t)$, $n = 1, \cdots, N_{gal}$ are the solutions of the dynamical system (32).

For boundary control problems, the more interesting case is the one where the Dirichlet boundary conditions $\vec{\boldsymbol{h}}(\vec{\boldsymbol{x}},t;d(t))$ defined by (27) depend on time t. In order to match these boundary conditions, Graham *et al.* (1999a), Ravindran (2000a,b) and Fahl (2000) propose to search the reduced order solution of the low-order dynamical system (32) as:

$$\vec{\boldsymbol{u}}_{DS}(\boldsymbol{x},t) = \langle \vec{\boldsymbol{u}}(\vec{\boldsymbol{x}},t)\rangle + \gamma(t)\vec{\boldsymbol{u}}_c(\vec{\boldsymbol{x}}) + \sum_{m=1}^{N_{gal}} a_{DS}^{(m)}(t)\vec{\boldsymbol{\Phi}}^{(m)}(\vec{\boldsymbol{x}}) \tag{38}$$

where $\vec{\boldsymbol{u}}_c(\vec{\boldsymbol{x}})$, $\vec{\boldsymbol{x}} \in \Omega$ is a reference flow field, describing how the control action $\gamma(t)\vec{\boldsymbol{c}}(\vec{\boldsymbol{x}})$, $\vec{\boldsymbol{x}} \in \Gamma_c$, $t \geq 0$ influences the flow and satisfying the following boundary conditions:

$$\gamma(t)\vec{\boldsymbol{u}}_c(\vec{\boldsymbol{x}}) = \begin{cases} \gamma(t)\vec{\boldsymbol{c}}(\vec{\boldsymbol{x}}), & \vec{\boldsymbol{x}} \in \Gamma_c,\ t \geq 0, \\ \vec{\boldsymbol{0}} & \vec{\boldsymbol{x}} \in \Gamma \setminus \Gamma_c,\ t \geq 0. \end{cases} \tag{39}$$

Similar to the procedure presented for the time-independent case, a mean velocity $\langle \vec{\boldsymbol{u}}(\vec{\boldsymbol{x}},t)\rangle$ is first computed as the ensemble average of the modified input data defined as $\mathcal{U}' = \{\vec{\boldsymbol{u}}(\vec{\boldsymbol{x}},t_1) - \gamma(t_1)\vec{\boldsymbol{u}}_c(\vec{\boldsymbol{x}}), \cdots, \vec{\boldsymbol{u}}(\vec{\boldsymbol{x}},t_{N_t}) - \gamma(t_{N_t})\vec{\boldsymbol{u}}_c(\vec{\boldsymbol{x}})\}$. Afterward, the POD basis functions are estimated with the input collection $\mathcal{U}'' = \{\vec{\boldsymbol{u}}(\vec{\boldsymbol{x}},t_1) - \gamma(t_1)\vec{\boldsymbol{u}}_c(\vec{\boldsymbol{x}}) - \langle \vec{\boldsymbol{u}}(\vec{\boldsymbol{x}},t)\rangle, \cdots, \vec{\boldsymbol{u}}(\vec{\boldsymbol{x}},t_{N_t}) - \gamma(t_{N_t})\vec{\boldsymbol{u}}_c(\vec{\boldsymbol{x}}) - \langle \vec{\boldsymbol{u}}(\vec{\boldsymbol{x}},t)\rangle\}$.

Since $(\vec{\boldsymbol{u}}(\vec{\boldsymbol{x}},t_i) - \gamma(t_i)\vec{\boldsymbol{u}}_c(\vec{\boldsymbol{x}}))|_{\Gamma_c} = \vec{\boldsymbol{0}}$ and $\langle \vec{\boldsymbol{u}}(\vec{\boldsymbol{x}},t)\rangle$ matches all other non homogeneous boundary conditions, the POD basis functions satisfy homogeneous boundary conditions on the whole domain. This approach is the one used in §8.5 to incorporate into the POD-based reduced order model the boundary control for the cylinder wake.

7.4 Application of POD/Galerkin to incompressible flows: Pressure Velocity formulation

In this section, we outline the procedure for deriving a POD based reduced order model in the case of incompressible flows. The motion of the fluid sat-

isfies the Navier-Stokes equations, written in a pressure-velocity formulation as:

$$\frac{\mathbb{D}\vec{\boldsymbol{u}}}{\mathbb{D}t} = -\vec{\boldsymbol{\nabla}}P + \frac{1}{Re}\vec{\boldsymbol{\Delta}}\vec{\boldsymbol{u}} \tag{40}$$

where $\mathbb{D}/\mathbb{D}t = \partial/\partial t + \vec{\boldsymbol{u}} \cdot \vec{\boldsymbol{\nabla}}$ is the material derivative. In equation (40), the velocities have been normalized by some velocity scale U, lengths by a length scale D, time by U/D, pressure by ρU^2 where ρ is the density, and Re is defined as usual, $Re = \rho UD/\mu$ where μ is the fluid's dynamic viscosity. The equations (40) may be written as

$$\dot{\vec{\boldsymbol{u}}} = \vec{\boldsymbol{N}}(\vec{\boldsymbol{u}}) - \vec{\boldsymbol{\nabla}}P \tag{41}$$

where $\vec{\boldsymbol{N}}(\vec{\boldsymbol{u}}) = -\left(\vec{\boldsymbol{u}} \cdot \vec{\boldsymbol{\nabla}}\right)\vec{\boldsymbol{u}} + \frac{1}{Re}\vec{\boldsymbol{\Delta}}\vec{\boldsymbol{u}}$.

For incompressible flows, each of the POD eigenfunctions satisfies the continuity equation (see Cordier and Bergmann, 2002, §5.5.2). It follows that equation (40) is the only one needed to prescribe the dynamics of the flow.

If we now introduce the development (28) into the Navier-Stokes equations (41), and take the inner products with $\vec{\boldsymbol{\Phi}}^{(n)}$, $n = 1, \cdots, N_{gal}$, we obtain:

$$\dot{a}^{(n)}(t) = \left(\vec{\boldsymbol{\Phi}}^{(n)}, \vec{\boldsymbol{N}}(\vec{\boldsymbol{u}})\right) - \left(\vec{\boldsymbol{\Phi}}^{(n)}, \vec{\boldsymbol{\nabla}}P\right) \tag{42}$$

The non linear terms on the right-hand side are equal to:

$$\left(\vec{\boldsymbol{\Phi}}^{(n)}, \vec{\boldsymbol{N}}(\vec{\boldsymbol{u}})\right) = \sum_{m=1}^{N_{gal}} B_{nm}a^{(m)}(t) + \sum_{m=1}^{N_{gal}}\sum_{k=1}^{N_{gal}} C_{nmk}a^{(m)}(t)a^{(k)}(t) \tag{43}$$

where

$$B_{nm} = \frac{1}{Re}\left(\vec{\boldsymbol{\Phi}}^{(n)}, \vec{\boldsymbol{\Delta}}\vec{\boldsymbol{\Phi}}^{(m)}\right) \quad ; \quad C_{nmk} = -\left(\vec{\boldsymbol{\Phi}}^{(n)}, \left(\vec{\boldsymbol{\Phi}}^{(m)} \cdot \vec{\boldsymbol{\nabla}}\right)\vec{\boldsymbol{\Phi}}^{(k)}\right) \tag{44}$$

The coefficients B_{nm} and C_{nmk} are constants (independent of time). Therefore, they can be determined once and for all before integrating the ODEs (42).

Exploiting the fact that the $\vec{\boldsymbol{\Phi}}^{(n)}$ are solenoidal fields ($\vec{\boldsymbol{\nabla}} \cdot \vec{\boldsymbol{\Phi}}^{(n)} = 0$), and using the divergence theorem, the pressure term on the right-hand side of (42) is easilly rewritten as:

$$\left(\vec{\boldsymbol{\Phi}}^{(n)}, \vec{\boldsymbol{\nabla}}P\right) = \int_\Omega \vec{\boldsymbol{\Phi}}^{(n)} \cdot \vec{\boldsymbol{\nabla}}P \, d\,\vec{\boldsymbol{x}} = \int_\Omega \vec{\boldsymbol{\nabla}} \cdot \left(P\vec{\boldsymbol{\Phi}}^{(n)}\right) = \int_{\partial\Omega} P\vec{\boldsymbol{\Phi}}^{(n)} \cdot \vec{\boldsymbol{n}} \, d\,S \tag{45}$$

where $\vec{n}$ is the external normal to $\partial\Omega$.

Hence the contribution of the pressure term can be evaluated easily as soon as the pressure is known on the domain boundary. However a number of flow configurations exists where the term (45) vanishes exactly. If the velocity is zero along the boundary (for instance at a wall, or in the far field of an open flow) or if the normal velocity component is zero, then the pressure term vanishes completely. The same result is obtained when the boundary conditions are periodic because in this case the contributions of the periodic parts of the boundary $\partial\Omega$ cancel each other (see Zhou and Sirovich, 1992, for example). If we consider only a limited portion on the whole flow (like the near wall region of a turbulent boundary layer considered in the study of Aubry *et al.*, 1988) then the pressure term represents the influence of the rest of the flow on the domain under study, and must be specified as a boundary condition. Aubry *et al.* (1988) cope with this problem by adding a model for the unknown pressure fluctuations at their upper boundary. However, there is case where the situation is much worse, in that the boundary condition that have to be applied are not even known. A possible solution is to use a vorticity-transport form of the Navier-Stokes equations for deriving the reduced order model. This approach is used by Rempfer (1996) to study the transition over a flat plate and is fully described in Cordier (1996).

8 An example: cylinder flow

8.1 Introduction

This section illustrates the potential gain that can be offered by the use of the Proper Orthogonal Decomposition for optimal control of fluid flows. Due to the nonlinearity of the Navier-Stokes equations, the minimization of a defined objective functionnal is necessarily an iterative procedure and therefore is computationaly intensive. For cutting down the cost of the flow solutions necessary at each iteration of the optimizer, a basic idea[13] is to replace the Navier-Stokes equations by a POD reduced order model.

[13]To reduce the CPU costs necessary to solve one iteration of the optimization problem, Gunzburger (2000) proposed two complementary approaches. The first is simply to improve the optimization algorithms. For example, Gunzburger suggested to use trust region/quasi-Newton methods and discussed in further details how the regularization of the functional to minimize can be used to reduce the number of optimization iterations. Homescu *et al.* (2002) and Li *et al.* (2002) followed this method and included a regularization term in their objective functionals to circumvent ill-posedness. The second approach is to cut down the cost of the flow solves. Gunzburger claimed that following nonfeasible paths to optimality can effect a substantial cost reduction when convergence is obtained.

For our presentation, we have chosen as configuration the incompressible unsteady wake flow behind a circular cylinder at $Re = 200$. This test problem, representative of general bluff body wakes, has the advantage of combining a simple geometry with a rich flow dynamics. Furthermore, the validation of the flow simulator presented in §8.2 will be greatly facilitated by the numerous results, both experimental and numerical, existing for the Karman vortex shedding. Here the objective of the optimization is to suppress the Karman vortex shedding in the wake of the cylinder by rotating the cylinder at a constant or time dependent angular velocity. This investigation of drag optimization was motivated in part by the experience of Tokumaru and Dimotakis (1991) where 80% of drag reduction was found for the controlled flow (see figure 12).

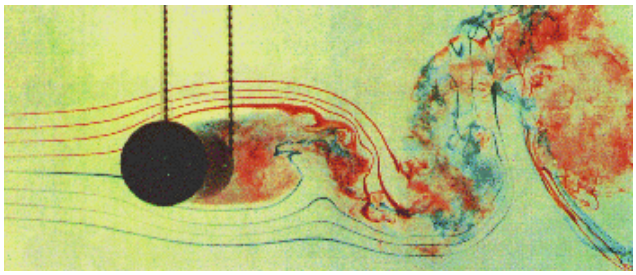

(a) Unforced flow.

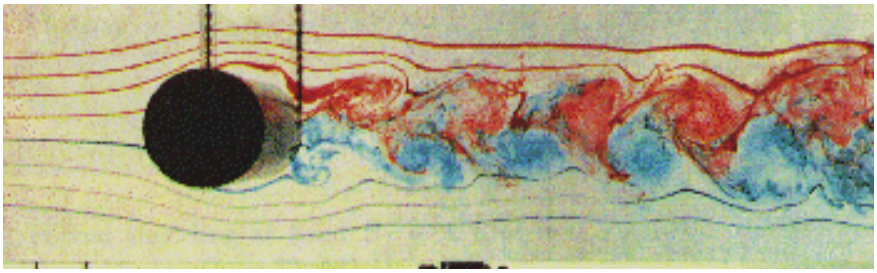

(b) Forced flow (80% drag reduction).

Figure 12: Flow visualizations from Tokumaru and Dimotakis (1991) ($Re = 15000$).

Recently, different approaches for the control of a flow around a cylinder have been succesfully employed. These approaches differ from the techniques used to control the flow, from the methods developed for deriving the adjoint

models necessary to estimate the cost function gradient and from the minimization algorithm. For example, He *et al.* (2000) and Homescu *et al.* (2002) achieved the control action, through cylinder rotation while Li *et al.* (2002) employed suction and blowing on the cylinder surface. In the following, to illustrate these lecture notes, we decide to resume the study of Graham *et al.* (1999a) where the reduced basis approach based on POD was used to control the wake flow at a Reynolds number of 100.

8.2 Numerical simulation of the cylinder flow

Here, we consider the channel flow past a circular cylinder of diameter D (see figure 13). Let Ω be a two-dimensional domain ($\Omega \subset \mathbb{R}^2$) filled with

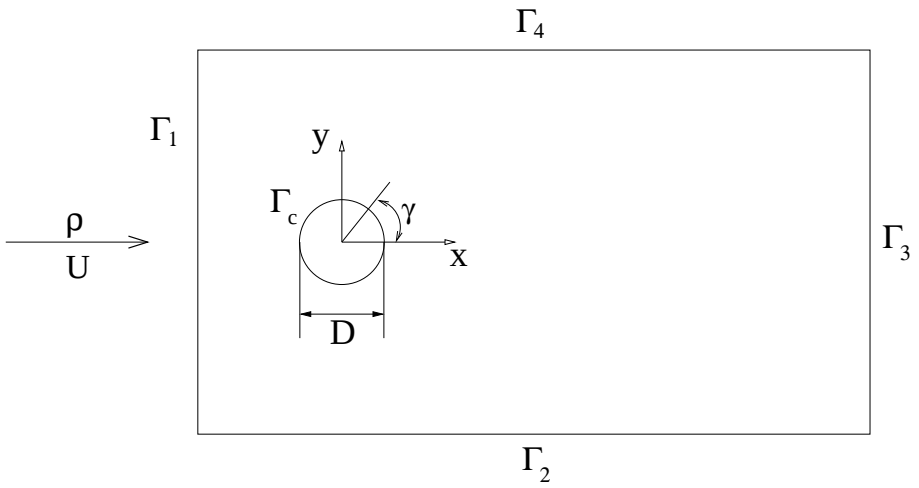

Figure 13: Simulation domain for circular cylinder flow problem.

a Newtonian incompressible viscous fluid of density ρ and viscosity μ. The boundaries $\partial\Omega$ of Ω are denoted by $\Gamma = \Gamma_1 \cup \Gamma_2 \cup \Gamma_3 \cup \Gamma_4 \cup \Gamma_c$ where Γ_i, $i = 1, 2, 3, 4$ correspond to the exterior domain and Γ_c to the cylinder boundary. The fluid is moving with velocity U in the x direction and the cylinder rotates counterclockwise with angular velocity γ. The continuity and Navier-Stokes equations are made dimensionless by introducing $L_{ref} = D$, $u_{ref} = U$, $t_{ref} = D/U$, $P_{ref} = \rho U^2$ as reference quantities for length, velocity, time and pressure. The governing equations can then be cast in the following non-dimensional form:

$$\vec{\boldsymbol{\nabla}} \cdot \vec{\boldsymbol{u}} = 0 \tag{46}$$

$$\frac{\partial \vec{\boldsymbol{u}}}{\partial t} + \left(\vec{\boldsymbol{u}} \cdot \vec{\boldsymbol{\nabla}}\right) \vec{\boldsymbol{u}} = -\vec{\boldsymbol{\nabla}} P + \frac{1}{Re} \vec{\boldsymbol{\Delta}}\, \vec{\boldsymbol{u}} \tag{47}$$

where $\vec{\boldsymbol{u}} = (u, v)$ are the two-dimensional velocity fields and $Re = \rho U D/\mu$ is the Reynolds number.

To complete equations (46) and (47), boundary conditions are now prescribed. At the left boundary, an inflow boundary condition is applied:

$$(u, v) = (1, 0) \quad \text{on} \quad \Gamma_1 \tag{48}$$

At the channel side-walls, zero shear stress conditions are imposed:

$$\frac{\partial u}{\partial y} = 0, \quad v = 0 \quad \text{on} \quad \Gamma_2, \Gamma_4 \tag{49}$$

Provided the boundary Γ_3 is placed at a sufficient distance downstream of the cylinder, the condition

$$P = 0 \quad \text{on} \quad \Gamma_3 \tag{50}$$

is found[14] to be an acceptable approximation for conditions at the outflow.

Finally, on the surface of the cylinder the velocity is equal to the speed of rotation $\vec{\boldsymbol{\Omega}} = (\Omega_x, \Omega_y)$:

$$(u, v) = (\Omega_x, \Omega_y) = (-\gamma y, \gamma x) \quad \text{on} \quad \Gamma_c \tag{51}$$

where $\gamma = 0$ for the uncontrolled flow.

8.2.1 Discretization of the equations

Equations (46) and (47) are now discretized[15] in time via a three step projection method (see Chorin, 1968; Jin and Braza, 1993) and in space using a Galerkin finite element approximation (see Zienkiewicz and Taylor, 2000).

[14] When this boundary condition is used, no spurious reflections from the downstream boundary appear, justifying a posteriori the choice of this outlet boundary condition (see §8.2.2 for numerical evidence).

[15] The method of time discretization used in this paper is somewhat different from the projection method employed by Graham *et al.* (1999a,b) and Morgan and Peraire (1998).

Time discretization A semi-implicit second-order accurate scheme in time is used (see Jin and Braza, 1993). An approximated velocity field $\vec{\boldsymbol{u}}^*$ is first determined at time step $(n+1)$ by using a guessed pressure field $P^* = P^n$:

$$\frac{\vec{\boldsymbol{u}}^* - \vec{\boldsymbol{u}}^n}{\Delta t} = -\left(\vec{\boldsymbol{u}}^n \cdot \vec{\boldsymbol{\nabla}}\right)\vec{\boldsymbol{u}}^* + \frac{1}{Re}\vec{\boldsymbol{\Delta}}\,\vec{\boldsymbol{u}}^* - \vec{\boldsymbol{\nabla}}P^n \tag{52}$$

where $\vec{\boldsymbol{u}}^n$ and P^n denote respectively $\vec{\boldsymbol{u}}(\vec{\boldsymbol{x}}, t^n)$ and $P(\vec{\boldsymbol{x}}, t^n)$ with $t^{n+1} = t^n + \Delta t$.

The true velocity field at the $(n+1)$ time step is then given by

$$\vec{\boldsymbol{u}}^{n+1} = \vec{\boldsymbol{u}}^* - \vec{\boldsymbol{\nabla}}\,\phi \tag{53}$$

where ϕ is an auxiliary potential function estimated by the Poisson equation

$$\Delta\,\phi = \vec{\boldsymbol{\nabla}} \cdot \vec{\boldsymbol{u}}^* \tag{54}$$

obtained by claiming $\vec{\boldsymbol{\nabla}} \cdot \vec{\boldsymbol{u}}^{n+1} = 0$.

The pressure at the $(n+1)$ time step is finally calculated by the simplified[16] equation:

$$P^{n+1} = P^n + \frac{\phi}{\Delta t} \tag{56}$$

Spatial discretization Equations (52), (53) and (54) are then discretized in space using the Galerkin finite element method (see Zienkiewicz and Taylor, 2000). The two-dimensional domain Ω is discretized into a mesh of triangular elements, and linear shape functions[17] $N_I(\vec{\boldsymbol{x}})$ where $\vec{\boldsymbol{x}} = (x, y)$ are defined for each vertex I. These shape functions may be used to approximate the problem variables $\vec{\boldsymbol{u}}$ and P at each time step in a piecewise linear fashion:

$$\vec{\boldsymbol{u}}(\vec{\boldsymbol{x}}) = \sum_{J=1}^{inode} \vec{\boldsymbol{u}}_{\boldsymbol{J}}\, N_J(\vec{\boldsymbol{x}}) \quad \text{or} \quad u_i(x,y) = \sum_{J=1}^{inode} u_{iJ}\, N_J(x,y) \quad i = 1,2 \tag{57}$$

$$P(\vec{\boldsymbol{x}}) = \sum_{J=1}^{inode} P_J\, N_J(\vec{\boldsymbol{x}}) \quad \text{or} \quad P(x,y) = \sum_{J=1}^{inode} P_J\, N_J(x,y) \tag{58}$$

[16] The true expression for the pressure field at the $(n+1)$ time step is:

$$\vec{\boldsymbol{\nabla}}P^{n+1} = \vec{\boldsymbol{\nabla}}\left(P^n + \frac{\phi}{\Delta t}\right) + \vec{\boldsymbol{\nabla}} \cdot \left(\vec{\boldsymbol{\nabla}}\phi \otimes \vec{\boldsymbol{u}}^n\right) - \frac{1}{Re}\vec{\boldsymbol{\Delta}}(\vec{\boldsymbol{\nabla}}\phi) \tag{55}$$

where $\otimes$ denotes the dyadic product. In Braza *et al.* (1990), it is shown that the expressions (55) and (56) give practically the same results for a moderate Reynolds number.

[17] The requirements that $N_I(\vec{\boldsymbol{x}})$ be one at the node I, zero at all the other nodes, and be piecewise linear in x and y coordinates over each triangular element are sufficient to specify it uniquely (see Zienkiewicz and Morgan, 1983).

where *inode* is the total number of vertices and $\vec{\boldsymbol{u}}_{\boldsymbol{J}}$ and P_J denote the values of the velocity and pressure at the mesh node J. Figure 14 shows the finite element mesh, consisting of 25042 triangles and 12686 vertices, used in this paper.

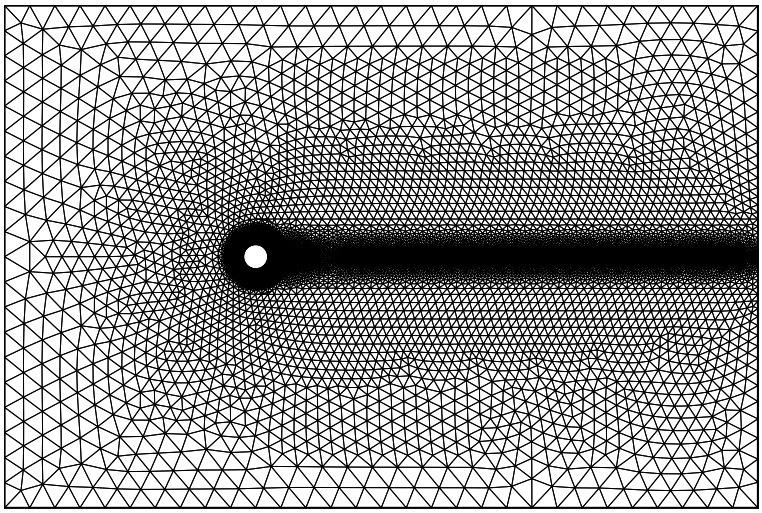

Figure 14: Finite element mesh (diameter of cylinder = 1 ; upstream and downstream boundaries from center of cylinder = 10, 20 ; Width = 20).

Then the time discretization equations (52), (53) and (54) are transformed via a Galerkin projection onto the linear shape functions $N_I(\vec{\boldsymbol{x}})$. Thus, for every node I in the mesh, equation (52) leads to

$$\begin{aligned}(N_I, \vec{\boldsymbol{u}}^* - \vec{\boldsymbol{u}}^n) = &- \Delta t \left(N_I, \left(\vec{\boldsymbol{u}}^n \cdot \vec{\boldsymbol{\nabla}}\right) \vec{\boldsymbol{u}}^*\right) \\ &+ \frac{\Delta t}{Re}\left[N_I \, \vec{\boldsymbol{\nabla}} \, \vec{\boldsymbol{u}}^*\right] - \frac{\Delta t}{Re}\left(\vec{\boldsymbol{\nabla}} \, N_I, \vec{\boldsymbol{\nabla}} \, \vec{\boldsymbol{u}}^*\right) \\ &- \Delta t \left(N_I, \vec{\boldsymbol{\nabla}} P^n\right)\end{aligned} \tag{59}$$

where

$$\left(\vec{\boldsymbol{a}}, \vec{\boldsymbol{b}}\right) = \int_\Omega \vec{\boldsymbol{a}} \cdot \vec{\boldsymbol{b}} \, d\Omega \quad ; \quad (\alpha, \vec{\boldsymbol{a}}) = \int_\Omega \alpha \vec{\boldsymbol{a}} \, d\Omega \quad ; \quad [\vec{\boldsymbol{a}}] = \int_{\Gamma_1 \cup \Gamma_2 \cup \Gamma_3 \cup \Gamma_4 \cup \Gamma_c} \vec{\boldsymbol{a}} \cdot \vec{\boldsymbol{n}} \, d\Gamma$$

The reader can note that the order of the derivatives in the viscous term have been reduced by use of the Green's formula[18]. Finally, after some ma-

[18] We remind the reader that for f and g two scalar functions of $\vec{\boldsymbol{x}}$, the Green's formula

nipulations, equation (59) is equivalent to:

$$\sum_{J=1}^{inode} \mathcal{M}_{IJ}(\vec{\boldsymbol{u}}_{\boldsymbol{J}}^{*} - \vec{\boldsymbol{u}}_{\boldsymbol{J}}^{n}) = \vec{\boldsymbol{f}}_{\boldsymbol{I}}^{1} \tag{61}$$

where $\mathcal{M}_{IJ} = (N_I, N_J)$ is the finite element consistent mass matrix and where $\vec{\boldsymbol{f}}_{\boldsymbol{I}}^{1}$ are defined by equation (85) in appendix A.

The Green's formula is also used to reduce the order of the derivatives appearing in the Galerkin projection of equation (54). It follows that the Galerkin form of the Poisson equation writes

$$(N_I, \Delta\,\phi) = \left[N_I\,\vec{\boldsymbol{\nabla}}\,\phi\right] - \left(\vec{\boldsymbol{\nabla}} N_I, \vec{\boldsymbol{\nabla}}\,\phi\right) = \left(N_I, \vec{\boldsymbol{\nabla}} \cdot \vec{\boldsymbol{u}}^{*}\right) \tag{62}$$

or, in an algebraic form, as the set of linear equations

$$\sum_{J=1}^{inode} \mathcal{K}_{IJ}\phi_J = f_I^2 \tag{63}$$

where $\mathcal{K}_{IJ} = (\vec{\boldsymbol{\nabla}} N_I, \vec{\boldsymbol{\nabla}} N_J)$ is the stiffness matrix. The left-hand side are defined by equation (86) in appendix A.

Finally, the Galerkin form of equation (53) is:

$$\sum_{J=1}^{inode} \mathcal{M}_{IJ}(\vec{\boldsymbol{u}}_{\boldsymbol{J}}^{n+1} - \vec{\boldsymbol{u}}_{\boldsymbol{J}}^{*}) = \vec{\boldsymbol{f}}_{\boldsymbol{I}}^{3} \tag{64}$$

where $\vec{\boldsymbol{f}}_{\boldsymbol{I}}^{3}$ are defined by equation (87) in appendix A.

The algebraic equations sets (61), (63) and (64) are now solved with the Partial Differential Equations Toolbox of Matlab.

---

is given by:

$$\int_{\Omega} \left(f\Delta g + \vec{\boldsymbol{\nabla}} f \cdot \vec{\boldsymbol{\nabla}} g\right)\, d\,\Omega = \int_{\Gamma} f \frac{d\,g}{d\,n}\, d\,\Gamma \tag{60}$$

where $\frac{d\,g}{d\,n} = \vec{\boldsymbol{\nabla}} g \cdot \vec{\boldsymbol{n}}$ is the normal derivative and $\vec{\boldsymbol{n}}$ the external normal of Γ.

8.2.2 Simulation results

The goal of these computational experiments[19] is to simulate the development of the Karman vortex shedding in the laminar wake of a stationary cylinder for a Reynolds number of 200. For this value of Reynolds number, a lot of results are available from previous investigations for comparison.

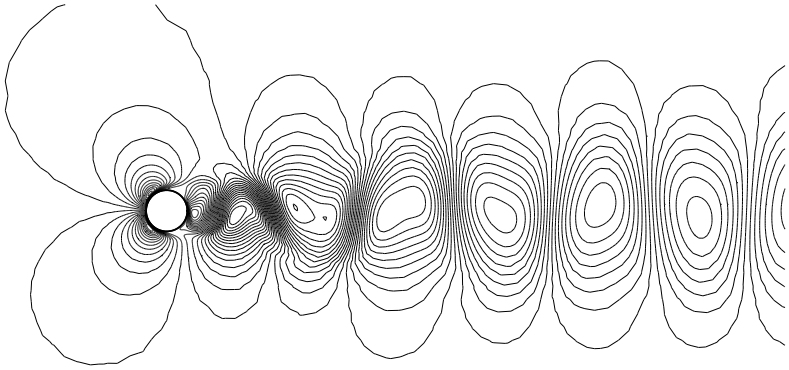

Figure 15: Iso-contours of the v velocity component for the stationary cylinder ($Re = 200$).

Figures 15 and 16 represent respectively a typical solution of the v velocity component and of the spanwise vorticity field obtained by our numerical simulation after all the transients have died out. These figures display well developed Karman vortex street and no spurious reflections from the downstream boundary are visible[20].

In a viscous flow the total forces acting on a body are contributed by the pressure and skin friction due to the viscous effects. Let K_p be the pressure coefficient defined by

$$K_p = \frac{P - P_\infty}{1/2\rho_\infty U_\infty^2} \ ,$$

where the subscript ∞ denotes quantities evaluated on the input boundary. The aerodynamic coefficients can then be calculated in a dimensionless form as:

$$\vec{\boldsymbol{C}} = \vec{\boldsymbol{C_P}} + \vec{\boldsymbol{C_f}} = (C_D, C_L) = -\int_{\Gamma_c} K_p \vec{\boldsymbol{n}} \, d\Gamma + \frac{2}{Re} \int_{\Gamma_c} \frac{\partial \vec{\boldsymbol{u}}}{\partial \vec{\boldsymbol{n}}} \, d\Gamma \qquad (65)$$

[19] Although these simulations are only two-dimensional and then lack of the three-dimensional effects of instabilities and turbulence, we claim that they can be representative of a great part of the physical phenomea responsible for drag reduction described in Tokumaru and Dimotakis (1991).

[20] This behavior is confirmed by contours of pressure field not represented here.

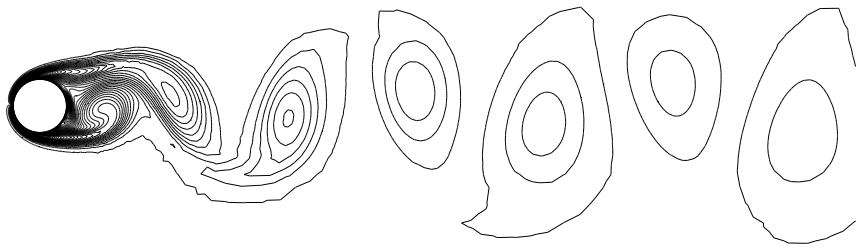

Figure 16: Iso-contours of the spanwise vorticity for the stationary cylinder ($Re = 200$).

where the subscripts P and f represent the contribution from pressure and friction, respectively. The two integrals over Γ_c appearing in (65) are straightforward to estimate given the nodal values of P and $\vec{\boldsymbol{u}}$.

Figure 17 shows plots of the time histories of the lift and drag coefficient C_L and C_D for the stationary cylinder when the non linear saturation is observed. The mean value of C_D is 1.3543 (see table 2) and the unsteady amplitude of C_L and C_D are 1.376 and 0.097 respectively. The periodic regime which is reached asymptotically is characterized by the frequency at which vortices are shed. However for comparison purposes, it was found convenient to introduce a non dimensional representation of the shedding frequency, the Strouhal number[21] defined as

$$St = \frac{f D}{U} \tag{66}$$

where f is the fundamental frequency obtained by a spectral analysis of the lift coefficient.

In table 1, a comparison is made between the Strouhal numbers from our numerical simulation and those obtained experimentally and computationally by various authors for the stationary cylinder at $Re = 200$. The agreement with all the previous experimental and computational data is very good. Similarly, in table 2, the time-averaged drag coefficient is seen to be in very good agreement with the results obtained previously. Therefore, as long as the value of the Reynolds number is low, our two-dimensional numerical simulation can be viewed to represent correctly the dynamics of the cylinder

[21] In this paper, the length and velocity reference quantities are $L_{ref} = D$ and $u_{ref} = U$ (see §8.2). It follows that the Strouhal number is confused with the fundamental frequency.

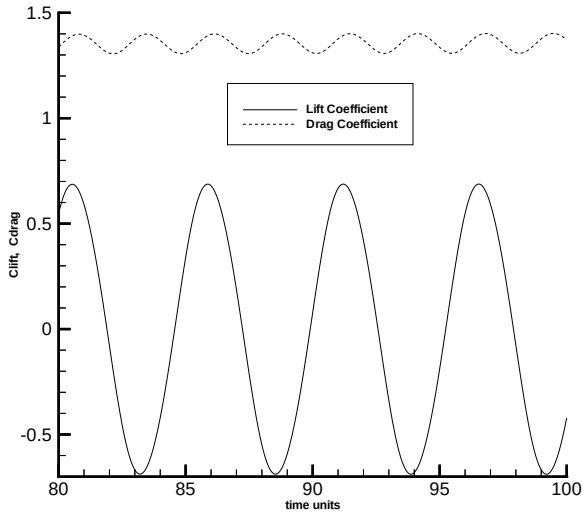

Figure 17: The variations of the lift and drag coefficients versus time for the stationary cylinder ($Re = 200$).

Re	Present work	He *et al.* (2000)	Henderson (1997)	Braza *et al.* (1986)
200	0.1918	0.1978	0.1971	0.20

Table 1: Comparison of Strouhal numbers for the stationary cylinder ($Re = 200$).

Re	Present work	He *et al.* (2000)	Henderson (1997)	Braza *et al.* (1986)
200	1.3543	1.3560	1.3412	1.39

Table 2: Comparison of the mean drag coefficients for the stationary cylinder ($Re = 200$).

flow. However, we have to keep in mind that for higher values of the Reynolds number, the three-dimensional phenomena become predominant. This characteristic explains the well-known overprediction of the drag coefficient for two-dimensional simulations (see He *et al.*, 2000).

8.3 POD of the stationary cylinder flow

Here we use the snapshot variant of Proper Orthogonal Decomposition (see Cordier and Bergmann, 2002, §5.4) to extract dominant energy-containing structures from flow field data. In §8.4, these energetic modes will be used to generate low-dimensional approximation of the Navier-Stokes equations by Galerkin Projection of the POD basis functions onto the governing[22] equations (46) and (47).

8.3.1 Algorithm for the computation of POD basis functions

Let $\vec{\boldsymbol{u}}(\vec{\boldsymbol{x}},t)$ be a given flow field and $\vec{\boldsymbol{u}}(\vec{\boldsymbol{x}},t_k)$, $k=1,\cdots N_t$ denote an ensemble of snapshots of the flow corresponding to N_t different time instances t_k.

The computation of the POD basis functions takes the following algorithmic form:

1. We decompose $\vec{\boldsymbol{u}}(\vec{\boldsymbol{x}},t)$ as follows

$$\vec{\boldsymbol{u}}(\vec{\boldsymbol{x}},t)=\vec{\boldsymbol{u}}_{\boldsymbol{m}}(\vec{\boldsymbol{x}})+\vec{\boldsymbol{v}}(\vec{\boldsymbol{x}},t)$$

   where:

$$\vec{\boldsymbol{u}}_{\boldsymbol{m}}(\vec{\boldsymbol{x}})=\frac{1}{N_t}\sum_{k=1}^{N_t}\vec{\boldsymbol{u}}(\vec{\boldsymbol{x}},t_k)$$

   is the flow mean value obtained as the arithmetic average of the snapshots.

2. We build the $N_t\times N_t$ correlation matrix C. The matrix elements of C are given by:

$$C_{kl}=\frac{1}{N_t}\left(\vec{\boldsymbol{v}}(\vec{\boldsymbol{x}},t_k),\vec{\boldsymbol{v}}(\vec{\boldsymbol{x}},t_l)\right)=\frac{1}{N_t}\int_\Omega \vec{\boldsymbol{v}}(\vec{\boldsymbol{x}},t_k)\cdot\vec{\boldsymbol{v}}(\vec{\boldsymbol{x}},t_l)\,d\vec{\boldsymbol{x}}$$

[22] Since the POD eigenfunctions are divergence free by construction, it will be useless in §8.4 to restrict the weak form of the continuity equation to the POD subspace. Here, the continuity equation is included to talk of generalities.

The inner products defining this correlation matrix are easily computed with the aid of the finite element mass matrix $\mathcal{M}$ as:

$$C_{kl} = \frac{1}{N_t} \sum_{J=1}^{inode} \sum_{K=1}^{inode} \vec{\boldsymbol{v}}_{\boldsymbol{J}}(t_k) \cdot \vec{\boldsymbol{v}}_{\boldsymbol{K}}(t_l)\, \mathcal{M}_{JK}$$

3. We solve the eigenvalue problem:

$$C\vec{\boldsymbol{A}} = \lambda \vec{\boldsymbol{A}} \ . \tag{67}$$

We recall that since C is a non-negative, hermitian matrix, it has a complete set of orthogonal eigenvectors $\vec{\boldsymbol{A}}^{(\mathbf{1})}, \cdots, \vec{\boldsymbol{A}}^{(\boldsymbol{N_t})}$:

$$\vec{\boldsymbol{A}}^{(\mathbf{1})} = \begin{bmatrix} A_1^{(1)} \\ A_2^{(1)} \\ \vdots \\ A_{N_t}^{(1)} \end{bmatrix}, \quad \vec{\boldsymbol{A}}^{(\mathbf{2})} = \begin{bmatrix} A_1^{(2)} \\ A_2^{(2)} \\ \vdots \\ A_{N_t}^{(2)} \end{bmatrix}, \quad \cdots, \quad \vec{\boldsymbol{A}}^{(\boldsymbol{N_t})} = \begin{bmatrix} A_1^{(N_t)} \\ A_2^{(N_t)} \\ \vdots \\ A_N^{(N_t)} \end{bmatrix}$$

with the corresponding eigenvalues arranged in ascending order as $\lambda^{(1)} \geq \lambda^{(2)} \geq \cdots \geq \lambda^{(N_t)} \geq 0$.

4. We obtain the POD basis vectors $\vec{\boldsymbol{\Psi}}^{(\boldsymbol{n})}(\vec{\boldsymbol{x}})$, $n = 1, \cdots, N_t$ using:

$$\vec{\boldsymbol{\Psi}}^{(\boldsymbol{n})}(\vec{\boldsymbol{x}}) = \frac{1}{N_t \lambda^{(n)}} \sum_{k=1}^{N_t} A_k^{(n)} \vec{\boldsymbol{v}}(\vec{\boldsymbol{x}}, t_k) \ . \tag{68}$$

As it was presented in Cordier and Bergmann (2002), the method of snapshot consists of expressing the spatial basis function $\vec{\boldsymbol{\Psi}}^{(\boldsymbol{n})}(\vec{\boldsymbol{x}})$ as a linear combination of the snapshots $\vec{\boldsymbol{v}}(\vec{\boldsymbol{x}}, t_k)$. Furthermore, if the coefficients of the linear combination are properly scaled then they are confused with the eigenvectors of the temporal correlation matrix C.

5. We can numerically check that the eigenfunctions $A_k^{(n)}$ are mutually orthogonal and that the spatial eigenfunctions $\vec{\boldsymbol{\Psi}}^{(\boldsymbol{n})}(\vec{\boldsymbol{x}})$ are pairwise orthonormal:

$$\frac{1}{N_t} \sum_{k=1}^{N_t} A_k^{(n)} A_k^{(m)} = \lambda^{(n)} \delta_{nm} \quad ; \quad \int_\Omega \vec{\boldsymbol{\Psi}}^{(\boldsymbol{n})}(\vec{\boldsymbol{x}}) \cdot \vec{\boldsymbol{\Psi}}^{(\boldsymbol{m})}(\vec{\boldsymbol{x}})\, d\vec{\boldsymbol{x}} = \delta_{nm}$$

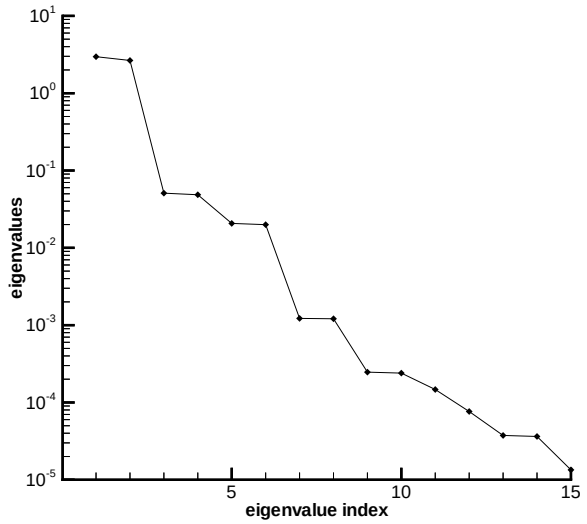

Figure 18: Eigenvalue spectrum for the stationary cylinder ($Re = 200$).

8.3.2 Eigenvalue spectrum and POD basis functions

Figure 18 shows the eigenvalue spectrum from the correlation matrix C formed from a set of 60 snapshots[23] of the cylinder flow, obtained at regular intervals over two vortex shedding periods. This eigenvalue spectrum plotted on a semi-log scale falls off rapidly. Hence as discussed in §3.4 of Cordier and Bergmann (2002), it seems possible to approximate with small error the correlation matrix C with a low-rank matrix. Moreover, the optimality of the POD basis functions (see Cordier and Bergmann, 2002, §4.3) suggest that the first[24] POD modes capture the most fluctuation kinetic energy possible in the average sense. Thus the claim that the decomposition of the flow in the POD basis functions is efficient for modelling the snapshots $\vec{\boldsymbol{v}}(\vec{\boldsymbol{x}}, t_k)$.

It is notable that these eigenvalues occur in pairs of almost equal values,

[23] It is well known (see Sirovich, 1987b) that the ensemble of snapshots can be augmented by exploiting the geometric symmetries of the problem, like the symmetry around the centerline of the cylinder flow; this would result in more accurate eigenfunction evaluation. The POD basis functions we computed here (see figures 19 and 20) very closely respected those symmetry properties without resorting to such a procedure. The role of symmetries in the POD methodology have been investigated in further details by Aubry *et al.* (1993).

[24] The number of POD modes to keep in the expansion will be clarified in §8.4 with the help of the relative information content (see figure 22).

whereas there is a large gap in magnitude between them. This pattern is in particular[25] identical to the one found in Graham *et al.* (1999a) for the cylinder flow and in Rempfer (1996) for the transitional boundary layer. The reason for this behaviour can be understood when we look at figures 19 and 21, where contours of velocity of the first two POD basis functions, $\vec{\mathbf{\Psi}}^{(1)}(\vec{x})$ and $\vec{\mathbf{\Psi}}^{(2)}(\vec{x})$, and the time behaviour of the corresponding expansion coefficients, $A_k^{(1)}$ and $A_k^{(2)}$ are shown. It can be seen that, essentially, the eigenfunctions of this pair are representing the same spatial structure, one of them just being shifted with respect to the other in the streamwise direction. Figure 21 shows that the corresponding expansion coefficients are analogously phase-shifted in time. Thus, if we multiply each of the eigenfunctions of such a pair by its corresponding expansion coefficient, we get a structure that is moving in the streamwise direction[26]. According to Rempfer and Fasel (1994), we can conclude that for our convective dominated flow, the coherent structure of order j is represented at the time step t_k by the following sum:

$$A_k^{(j)}\vec{\mathbf{\Psi}}^{(j)}(\vec{x}) + A_k^{(j+1)}\vec{\mathbf{\Psi}}^{(j+1)}(\vec{x})$$

where pairs[27] of eigenfunctions appear. In Aubry *et al.* (1992), the near degeneracy of the eigenvalue problem (67) was further studied. It was shown that this behaviour is a direct consequence of the presence of travelling waves in our flow. For the case of a parallel flow where structures of constant shape are travelling downstream at a constant speed, the eigenvalue problem would be degenerate, yielding pairs of identical eigenvalues.

The velocity contours of the third and fourth most energetic eigenmodes of the stationary cylinder flow are represented in figure 20. The same behaviour as already described for the first and second POD mode is still observed. The two POD basis functions form a pair of similar patterns, one shifted spatially with respect to the other.

The amplitudes of the first six temporal eigenfunctions $A_k^{(n)}$ are now plotted in figure 21. From this figure, it is clear that the basis functions corre-

[25] For the reasons explained in the following, this characteristic is common to many POD applications. Therefore, we choose randomly two bibliographic references.

[26] The same result can be easily obtained with the Fourier modes (see Cazemier *et al.*, 1998, p. 1691). It is sufficient to note that $\sin(x)$ and $\cos(x)$ form a pair of functions which differ by a shift over one quarter of their period and that the expression $a\cos(x) + b\sin(x) = (a^2+b^2)^{1/2}\cos(x \pm \delta)$ with $\tan(\delta) = \mp a/b$ provides the construction for a complete description of the evolution of a cosine wave.

[27] An immediate consequence is that it seems preferable to keep in the POD reduced order model developed in §8.4 an even number of POD modes.

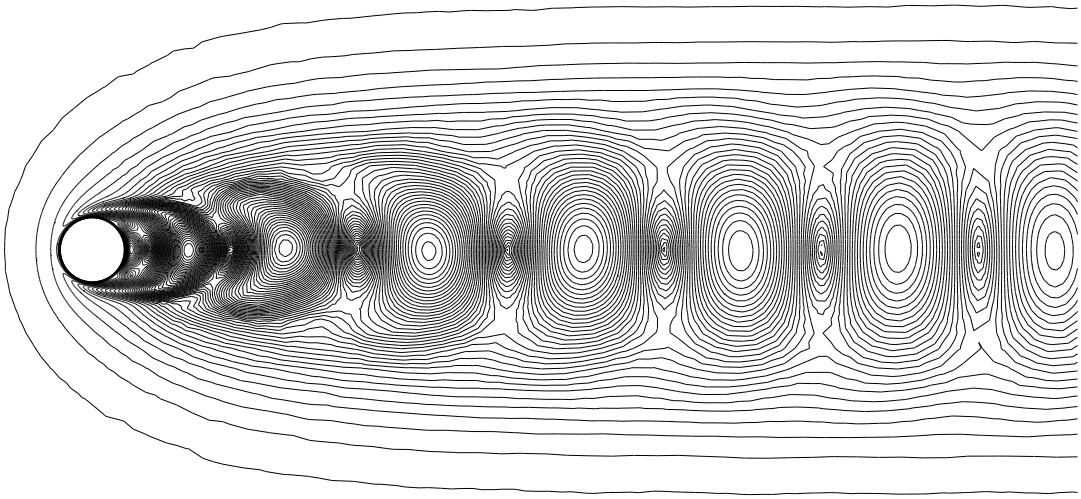

(a) First velocity mode $\vec{\mathbf{\Psi}}^{(1)}(\vec{x})$.

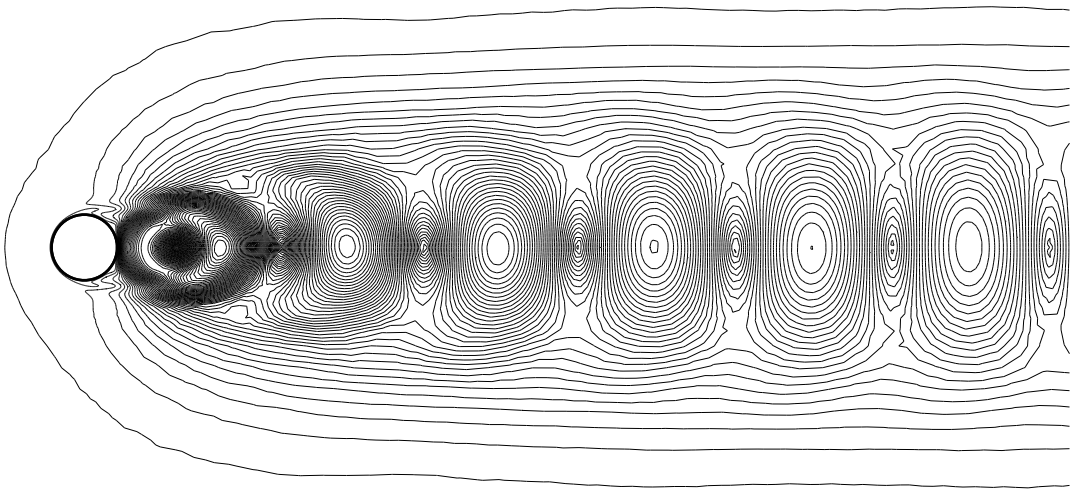

(b) Second velocity mode $\vec{\mathbf{\Psi}}^{(2)}(\vec{x})$.

Figure 19: Contours of velocity magnitude for the first two POD modes.

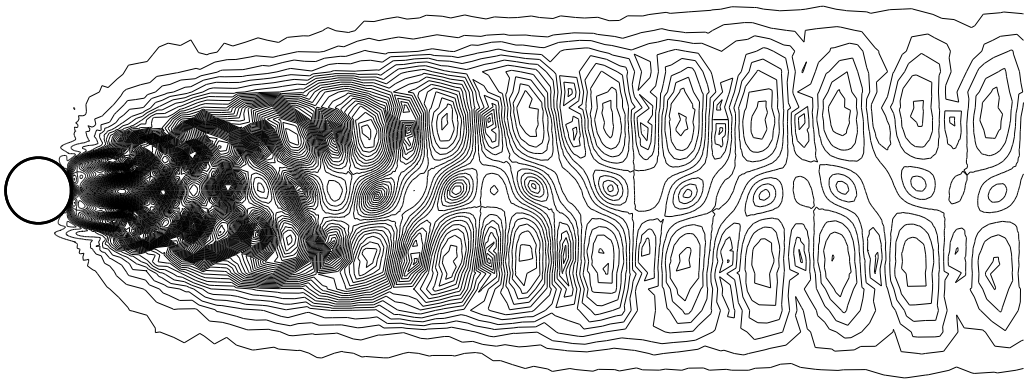

(a) Third velocity mode $\vec{\mathbf{\Psi}}^{(3)}(\vec{x})$.

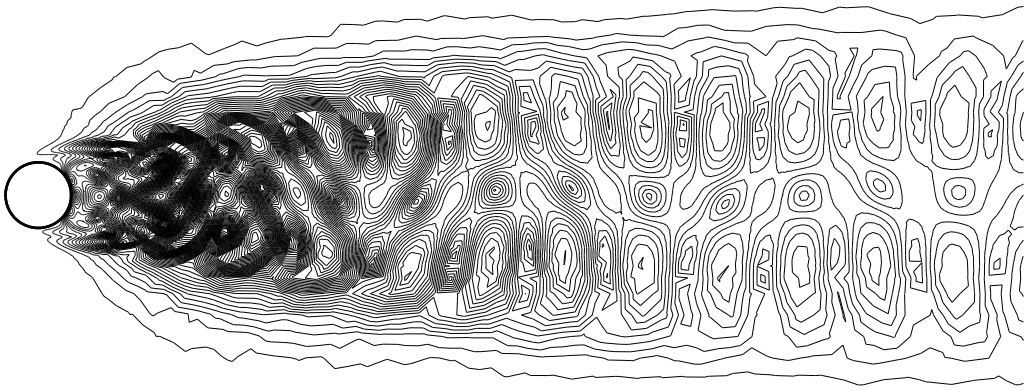

(b) Fourth velocity mode $\vec{\mathbf{\Psi}}^{(4)}(\vec{x})$.

Figure 20: Contours of velocity magnitude for the third and fourth POD modes.

spond very closely to the coefficients of a temporal Fourier series expansion for a periodic flow. For our flow configuration (convective dominated flow and low value of the Reynolds number), it is remarkably close to being so, even for the higher basis functions coefficients. As a direct consequence, the mean flow (the zero'th Fourier coefficient) would be (very nearly) found as the first POD mode if the correlation matrix C was formed without first subtracting it from the snapshots. For example, this result is observed in Rempfer and Fasel (1994) and Cordier (1996) where the first POD mode is virtually indistinguishable from the mean temporal flow when POD is not applied to the fluctuations $\vec{\boldsymbol{v}}(\vec{\boldsymbol{x}}, t)$ around the mean flow $\vec{\boldsymbol{u}}_{\boldsymbol{m}}(\vec{\boldsymbol{x}})$ but directly to the flow realizations $\vec{\boldsymbol{u}}(\vec{\boldsymbol{x}}, t)$.

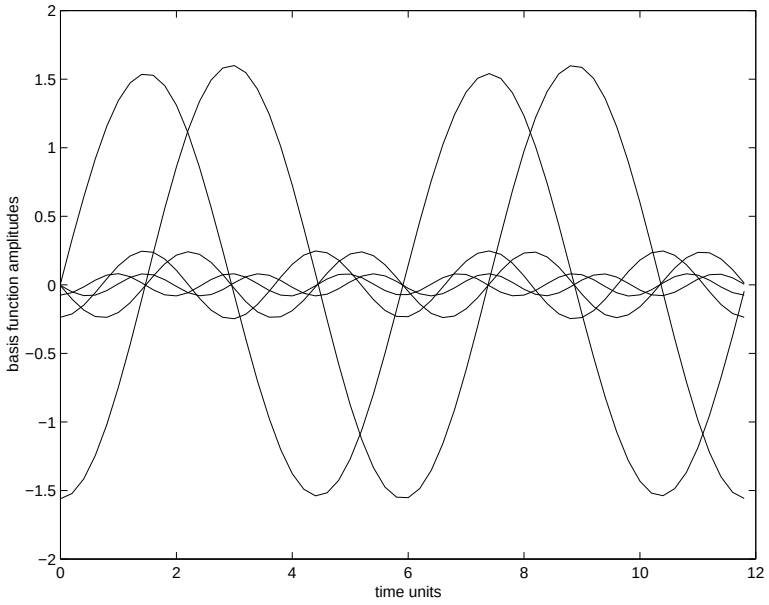

Figure 21: Mode amplitude for the first six modes.

Finally, the eigenvalue spectrum is in good agreement with those found previously by Deane *et al.* (1991), Gillies (1988) and Graham *et al.* (1999a) for an identical configuration. The associated spatial temporal POD basis functions also correspond satisfactorily.

8.4 POD Reduced Order Model for the stationary cylinder flow

In this section, we consider the construction of the POD reduced order model for the stationary flow (see §7.2). This model is based on a Galerkin projec-

tion of the Navier-Stokes equations (47) onto a space D_M^{POD} spanned by the M first POD basis functions.

8.4.1 Algorithm for the POD Reduced Order Model

Let $D^{POD} = \text{span}\{\vec{\mathbf{\Psi}}^{(1)}, \vec{\mathbf{\Psi}}^{(2)}, \cdots, \vec{\mathbf{\Psi}}^{(N_t)}\}$ denote the POD subspace determined in §8.3.

The development of the POD reduced order model takes the following algorithmic form:

1. In order to obtain a low-dimensional basis for the Galerkin projection, POD modes corresponding to small eigenvalues are neglected. To make this idea more precise, we define the relative information content[28] of the basis by:

$$RIC(M) = \frac{\sum_{k=1}^{M} \lambda^{(k)}}{\sum_{k=1}^{N_t} \lambda^{(k)}} \tag{69}$$

   If the basis is required that contains $\delta\%$ of the total energy initially contained in the flow, the dimension $M \ll N_t$ of the subspace D_M^{POD} of projection of the governing equations is the smallest integer M such that the information content is greater than δ.

2. We define $D_M^{POD} = \text{span}\{\vec{\mathbf{\Psi}}^{(1)}, \vec{\mathbf{\Psi}}^{(2)}, \cdots, \vec{\mathbf{\Psi}}^{(M)}\}$ and expand each velocity $\vec{\boldsymbol{u}}$ in terms of the POD modes as:

$$\vec{\boldsymbol{u}}(\vec{\boldsymbol{x}}, t) = \vec{\boldsymbol{u}}_{\boldsymbol{m}}(\vec{\boldsymbol{x}}) + \sum_{n=1}^{M} a^{(n)}(t)\, \vec{\mathbf{\Psi}}^{(n)}(\vec{\boldsymbol{x}}) \tag{70}$$

   where $\vec{\boldsymbol{u}}_{\boldsymbol{m}}(\vec{\boldsymbol{x}})$ is the mean velocity.

3. After plugging in the development of each velocity field $\vec{\boldsymbol{u}}$ into the Navier-Stokes equations (47), we restrict the weak form of the Navier-Stokes equations to D_M^{POD} and then solve for $a^{(n)}(t)$, $n = 1, \cdots, M$.

[28] The reader should remind that we already used in §3.2.1 and §4.2.1 the relative information content to study for the plane mixing layer the convergence of the scalar-PODs and the snapshot POD respectively. Moreover, this notion was introduced in §3.6 of Cordier and Bergmann (2002) to determine how many Singular Value Decomposition modes are necessary to get a good low-rank approximation of the original images.

Since the POD basis functions $\vec{\mathbf{\Psi}}^{(n)}$ are divergence free by construction, the continuity equation (46) is automatically verified by the POD eigenfunctions. It follows that it is useless to restrict the weak form of the continuity equation to D_M^{POD}.

8.4.2 Dynamical prediction via the Reduced Order Model

In figure 22, the relative information content defined by equation (69) is shown for the stationary flow cylinder. We obtain a confirmation of the fast convergence of the POD basis functions in terms of energy representation as early reported in §8.3.2 describing the eigenvalue spectrum (figure 18). We find out that the first six POD modes contain more that 99.9% of the flow kinetic energy ($RIC(6) = 99.94\%$). It follows that the dimension of the projection subspace is fixed to $M = 6$ as it was done previously in Deane *et al.* (1991) and Graham *et al.* (1999a).

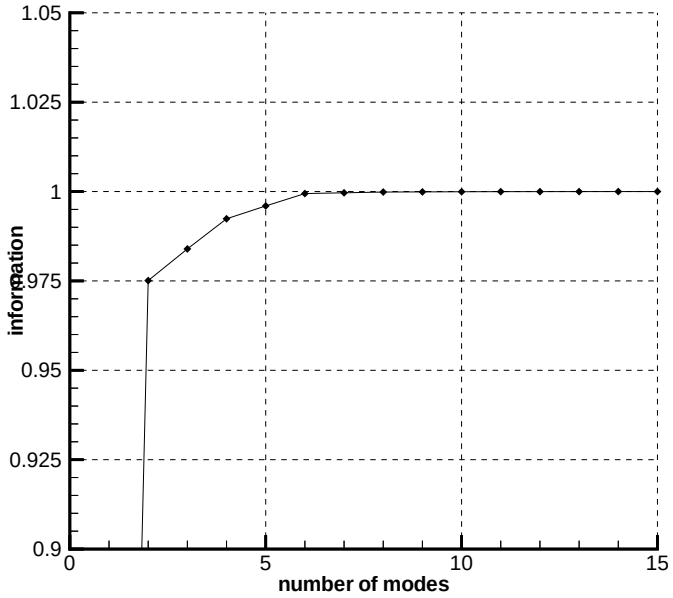

Figure 22: Relative information content for the stationary flow ($Re = 200$). $RIC(1) = 0.5148$.

The weak form of the Navier-Stokes equations (47) is then restricted to D_M^{POD}. It yields:

$$\left(\vec{\mathbf{\Psi}}^{(n)}, \frac{\partial \vec{u}}{\partial t} + \left(\vec{u} \cdot \vec{\nabla}\right) \vec{u}\right) = -\left(\vec{\mathbf{\Psi}}^{(n)}, \vec{\nabla} P\right) + \frac{1}{Re}\left(\vec{\mathbf{\Psi}}^{(n)}, \vec{\Delta}\, \vec{u}\right) \quad n = 1, \cdots, M \tag{71}$$

At this point it is important to note that the POD basis functions $\vec{\Psi}^{(n)}$ are divergence free as flow is incompressible and satisfy $\vec{\Psi}^{(n)} \cdot \vec{n} = 0$ on the surfaces Γ_1, Γ_2, Γ_4 and Γ_c. Combining these properties and the boundary condition $P = 0$ on Γ_3, we find that the pressure term vanishes exactly. Finally, the Galerkin approximation (71) to the Navier-Stokes equations is reduced to:

$$\left(\vec{\Psi}^{(n)}, \frac{\partial \vec{u}}{\partial t} + \left(\vec{u} \cdot \vec{\nabla}\right) \vec{u}\right) = -\frac{1}{Re}\left(\vec{\Delta}\,\vec{\Psi}^{(n)}, \vec{\Delta}\,\vec{u}\right) + \frac{1}{Re}\left[\vec{\Psi}^{(n)}\,\vec{\Delta}\,\vec{u}\right] \quad (72)$$

where $n = 1, \cdots, M$.

Equation (70) is then substituted into (72). After algebraic manipulations, we found the following set of evolution equations for the mode amplitudes $a^{(n)}(t)$:

$$\boxed{\frac{d\,a^{(n)}(t)}{d\,t} = A_n + \sum_{m=1}^{M} B_{nm}\,a^{(m)}(t) + \sum_{m=1}^{M}\sum_{k=1}^{M} C_{nmk}\,a^{(m)}(t)a^{(k)}(t)} \quad (73)$$

where the coefficients A_n, B_{nm}, C_{nmk} are given by:

$$A_n = -\left(\vec{\Psi}^{(n)}, \left(\vec{u}_{\boldsymbol{m}} \cdot \vec{\nabla}\right) \vec{u}_{\boldsymbol{m}}\right) - \frac{1}{Re}\left(\vec{\nabla}\vec{\Psi}^{(n)}, \vec{\nabla}\vec{u}_{\boldsymbol{m}}\right) + \frac{1}{Re}\left[\vec{\Psi}^{(n)}\,\vec{\nabla}\vec{u}_{\boldsymbol{m}}\right] \quad (74)$$

$$\begin{aligned} B_{nm} = &-\left(\vec{\Psi}^{(n)}, \left(\vec{u}_{\boldsymbol{m}} \cdot \vec{\nabla}\right) \vec{\Psi}^{(m)}\right) - \left(\vec{\Psi}^{(n)}, \left(\vec{\Psi}^{(m)} \cdot \vec{\nabla}\right) \vec{u}_{\boldsymbol{m}}\right) \\ &- \frac{1}{Re}\left(\vec{\nabla}\vec{\Psi}^{(n)}, \vec{\nabla}\vec{\Psi}^{(m)}\right) + \frac{1}{Re}\left[\vec{\Psi}^{(n)}\,\vec{\nabla}\vec{\Psi}^{(m)}\right] \end{aligned} \quad (75)$$

$$C_{nmk} = -\left(\vec{\Psi}^{(n)}, \left(\vec{\Psi}^{(m)} \cdot \vec{\nabla}\right) \vec{\Psi}^{(k)}\right) \quad (76)$$

The system (73) is the reduced order model of the uncontrolled flow. The inhomogeneous terms A_n, $n = 1, \cdots, M$ result from the contribution of the mean velocity $\vec{u}_{\boldsymbol{m}}(\vec{x})$ in equation (70).

The striking feature of this procedure is the significant decrease of complexity achieved in comparison to the original system. We transform a high-order dimensional PDE model (12686 vertices in the finite element formulation) to a low-order dimensional ODE model (6 POD modes kept in (73)).

The coefficients A_n, B_{nm}, C_{nmk} are determined once for all using the POD basis functions. The inner products appearing in the coefficients are easily computed, with the aid of the finite element consistent mass matrix $\mathcal{M}$.

The system of equations (73) is then integrated with a fourth order Runge-Kutta scheme from a given set of initial conditions

$$a^{(n)}(t=0) = \left(\left(\vec{\boldsymbol{u}}(\vec{\boldsymbol{x}}, t=0) - \vec{\boldsymbol{u}}_{\boldsymbol{m}}(\vec{\boldsymbol{x}}) \right), \vec{\boldsymbol{\Psi}}^{(\boldsymbol{n})} \right) \tag{77}$$

yielding a set of predicted time histories for the mode amplitudes $a^{(n)}(t)$ which can be compared with the temporal eigenfunctions[29] of the POD.

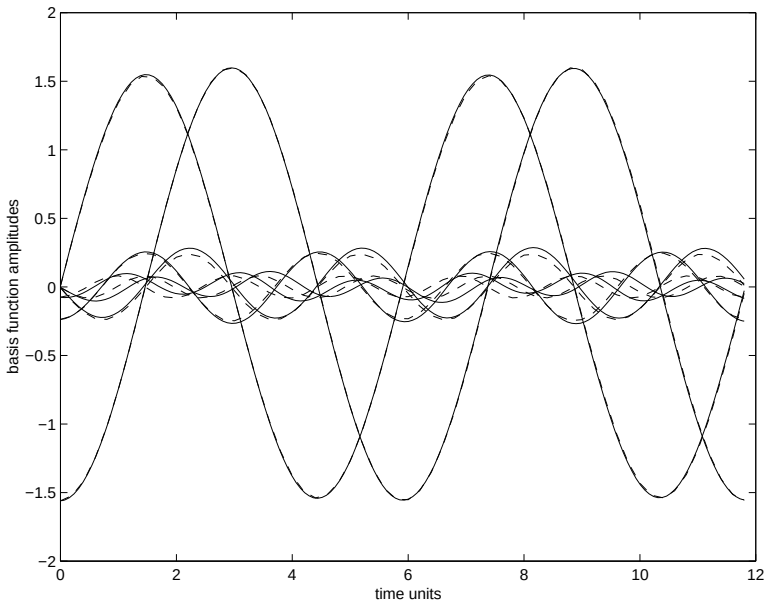

Figure 23: Predicted and projected mode amplitudes. Stationary cylinder flow. Solid line: predictions, dotted line: projections.

As shown in figure 23, excellent qualitative and quantitative agreement are found between the integrated time histories for the first two modes and the results obtained by the numerical simulation. For the higher POD modes, the amplitudes are only slightly less accurately predicted. We conclude that

[29]Due to the introduction of scaling factors in the linear combinations (68) defining the spatial eigenfunctions for the snapshot POD, there is no difference between the temporal eigenfunctions $A_k^{(n)}$ and the projection of the snapshots onto the spatial eigenfunctions $\left(\left(\vec{\boldsymbol{u}}(\vec{\boldsymbol{x}}, t_k) - \vec{\boldsymbol{u}}_{\boldsymbol{m}}(\vec{\boldsymbol{x}}) \right), \vec{\boldsymbol{\Psi}}^{(\boldsymbol{n})} \right)$, $k = 1, \cdots, N_t$.

a 6 mode model provides an entirely satisfactory description of the long term dynamics of the uncontrolled flow. The same results were obtained previously by Deane *et al.* (1991) and Graham *et al.* (1999a) with a similar configuration.

8.5 POD Reduced Order Model for the controlled flow

Here, we present a logical extension of the approach described in §8.4 to situations where the flow is controlled via cylinder rotation. Since the cylinder is now rotating, the boundary conditions on Γ_c become inhomogeneous and time-dependent. Therefore, the velocity expansion (70) is no longer valid for $\vec{\boldsymbol{u}}$ and the procedure described at the end of §7.3 need to be applied. In this method[30] called *control function method* by Graham *et al.* (1999a), the velocity expansion is now defined as

$$\vec{\boldsymbol{u}}(\vec{\boldsymbol{x}},t) = \vec{\boldsymbol{u}}_{\boldsymbol{m}}(\vec{\boldsymbol{x}}) + \gamma(t)\vec{\boldsymbol{u}}_{\boldsymbol{c}}(\vec{\boldsymbol{x}}) + \sum_{n=1}^{N_{POD}} a^{(n)}(t)\,\vec{\boldsymbol{\Psi}}^{(n)}(\vec{\boldsymbol{x}}) \tag{78}$$

where $\vec{\boldsymbol{u}}_{\boldsymbol{c}}(\vec{\boldsymbol{x}})$ is an arbitrary control function satisfying homogeneous boundary conditions. A convenient way to generate it is to take the solution for the steady cylinder rotation with $\gamma = 1$. Then the modified snapshots are defined as

$$\vec{\boldsymbol{u}}(\vec{\boldsymbol{x}},t_k) - \gamma(t_k)\vec{\boldsymbol{u}}_{\boldsymbol{c}}(\vec{\boldsymbol{x}}) \qquad k = 1,\cdots,N_t \tag{79}$$

and the algorithm described in §8.3.1 is used to determine the POD basis functions. By construction, these eigenfunctions $\vec{\boldsymbol{\Psi}}^{(n)}(\vec{\boldsymbol{x}})$ have now zero boundary conditions on the Dirichlet boundaries.

Inserting the expansion (78) into the Galerkin projection (72) of the Navier-Stokes equations, we obtain the reduced order control model:

$$\begin{aligned}\frac{d\,a^{(n)}(t)}{d\,t} =& A_n + \sum_{m=1}^{N_{gal}} B_{nm}\,a^{(m)}(t) + \sum_{m=1}^{N_{gal}}\sum_{k=1}^{N_{gal}} C_{nmk}\,a^{(m)}(t)a^{(k)}(t) \\ &+ D_n\,\frac{d\,\gamma}{dt} + \left(E_n + \sum_{m=1}^{N_{gal}} F_{nm}a^{(m)}(t)\right)\gamma(t) + G_n\gamma^2(t)\end{aligned} \tag{80}$$

[30] Another method called the "penalty method" is presented in Graham *et al.* (1999a). In this approach, the uncontrolled POD basis functions are retained and the inhomogeneous boundary conditions are imposed in a weak sense when performing the Galerkin Projection. This method is not used in this paper.

where A_n, B_{nm}, C_{nmk} are defined respectively by equations (74), (75), (76) and with:

$$D_n = -\left(\vec{\boldsymbol{\Psi}}^{(n)}, \vec{\boldsymbol{u}}_{\boldsymbol{c}}\right) \tag{81}$$

$$\begin{aligned} E_n = &-\left(\vec{\boldsymbol{\Psi}}^{(n)}, \left(\vec{\boldsymbol{u}}_{\boldsymbol{m}} \cdot \vec{\boldsymbol{\nabla}}\right) \vec{\boldsymbol{u}}_{\boldsymbol{c}}\right) - \left(\vec{\boldsymbol{\Psi}}^{(n)}, \left(\vec{\boldsymbol{u}}_{\boldsymbol{c}} \cdot \vec{\boldsymbol{\nabla}}\right) \vec{\boldsymbol{u}}_{\boldsymbol{m}}\right) \\ &- \frac{1}{Re}\left(\vec{\boldsymbol{\nabla}}\vec{\boldsymbol{\Psi}}^{(n)}, \vec{\boldsymbol{\nabla}}\vec{\boldsymbol{u}}_{\boldsymbol{c}}\right) + \frac{1}{Re}\left[\vec{\boldsymbol{\Psi}}^{(n)}\, \vec{\boldsymbol{\nabla}}\vec{\boldsymbol{u}}_{\boldsymbol{c}}\right] \end{aligned} \tag{82}$$

$$F_{nm} = -\left(\vec{\boldsymbol{\Psi}}^{(n)}, \left(\vec{\boldsymbol{\Psi}}^{(m)} \cdot \vec{\boldsymbol{\nabla}}\right) \vec{\boldsymbol{u}}_{\boldsymbol{c}}\right) - \left(\vec{\boldsymbol{\Psi}}^{(n)}, \left(\vec{\boldsymbol{u}}_{\boldsymbol{c}} \cdot \vec{\boldsymbol{\nabla}}\right) \vec{\boldsymbol{\Psi}}^{(m)}\right) \tag{83}$$

$$G_n = -\left(\vec{\boldsymbol{\Psi}}^{(n)}, \left(\vec{\boldsymbol{u}}_{\boldsymbol{c}} \cdot \vec{\boldsymbol{\nabla}}\right) \vec{\boldsymbol{u}}_{\boldsymbol{c}}\right) \tag{84}$$

Given initial conditions and a prescribed time history for γ, the system of equations (80) can be integrated forwards to yield predicted flow fields. Here, the cylinder is driven at an angular velocity $\gamma(t) = A \sin(2\pi S_t\, t)$ where $A = 3$ and $S_t = 0.75$. The results of twelve mode integrations (99% of the total energy) of the low order system (80), and the projections of the simulation onto the basis functions, are plotted in figure 24. The predictions of the controlled reduced order model are comparable to the stationary cylinder results (see section 8.4.2).

In conclusion, this approach is extremely attractive for optimal control problems governed by PDEs since it leads in general to high-fidelity reduced order control models more tractable to numerical approaches. POD reduced order models are particularly suited to gain CPU time in an optimization problem where in general a large-scale system has to be solved repeatedly. Recently, we applied this approach to control the cylinder wake flow (see Bergmann *et al.*, 2003). Our objective was to minimize the wake unsteadiness by sinusoidal rotation of the cylinder around ist principal axis. A reduced-order model based on POD was first built for the controlled flow. Then, following the method introduced by Ravindran (2000a), this reduced-order model was used as the state equations in the optimality system derived to estimate the flow control parameters.

A Discretized forms of equations (52), (53) and (54)

Since the projection method used in §8.2 is different than the one employed in Graham *et al.* (1999a,b) and Morgan and Peraire (1998), the left-hand

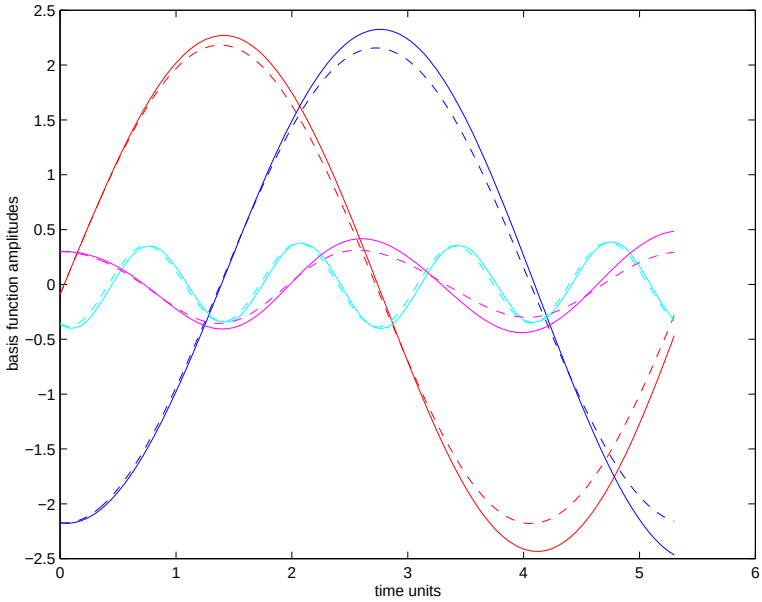

Figure 24: Predicted and projected mode amplitudes. Controlled flow ($A = 3\,;\ S_t = 0.75$). Solid line: predictions, dotted line: projections.

sides $\vec{\boldsymbol{f}}^{\boldsymbol{1}}_{\boldsymbol{I}}$, f^2_I and f^3_{iI} of equations (52), (53) and (54) respectively are not equal to those found in §9.2 of Morgan and Peraire (1998). Here, these terms are given by the following equations:

$$\begin{aligned}\vec{\boldsymbol{f}}^{\boldsymbol{1}}_{\boldsymbol{I}} = &-\Delta t \sum_{j=1}^{3}\sum_{J=1}^{inode}\sum_{K=1}^{inode}\left[\int_\Omega N_I N_J \frac{\partial N_K}{\partial x_j}\,d\,\Omega\right] u^n_{jJ}\vec{\boldsymbol{u}}^{\boldsymbol{*}}_{\boldsymbol{K}} \\ &+\frac{\Delta t}{Re}\sum_{J=1}^{inode}\left[\int_\Gamma N_I \frac{d\,N_J}{d\,n}\,d\,\Gamma - K_{IJ}\right]\vec{\boldsymbol{u}}^{\boldsymbol{*}}_{\boldsymbol{J}} \\ &-\Delta t\sum_{J=1}^{inode}\left(\int_\Omega N_I \vec{\boldsymbol{\nabla}} N_J\,d\,\Omega\right) P^n_J\end{aligned} \tag{85}$$

$$f^2_I = \sum_{J=1}^{inode}\int_\Gamma N_I \frac{d\,N_J}{d\,n}\,d\,\Gamma - \sum_{j=1}^{3}\sum_{J=1}^{inode}\left(\int_\Omega N_I \frac{\partial N_J}{\partial x_j} d\,\Omega\right) u^*_{jJ} \tag{86}$$

$$f^3_{iI} = -\sum_{J=1}^{inode}\left(\int_\Omega N_I \frac{\partial N_J}{\partial x_i} d\,\Omega\right)\phi_J \quad i = 1, 2 \tag{87}$$

References

Alexandrov N., Dennis Jr J.E., Lewis R.M. and Torczon V. (1997): A Trust Region framework for managing the use of approximation models in optimization. *Icase report*, N°. 97-50. Downloadable in http://www.icase.edu/library/reports/rdp/1997.html.

Alexandrov N.M., Lewis R.M., Gumbert C.R., Green L.L. and Newman P.A. (1999): Optimization with variable-fidelity models applied to wing design. *Icase report*, N°. 99-49. Downloadable in http://www.icase.edu/library/reports/rdp/1999.html.

Aubry N., Guyonnet R. and Lima R. (1992): Spatio-temporal symmetries and bifurcations via bi-orthogonal decompositions. *J. Nonlin. Sci.*, **2**, pp. 183-215.

Aubry N., Holmes P., Lumley J.L. and Stone E. (1988): The dynamics of coherent structures in the wall region of a turbulent boundary layer. *J. Fluid Mech.*, **192**, pp. 115-173.

Aubry N., Lian W. and Titi E. (1993): Preserving symmetries in the Proper Orthogonal Decomposition. *SIAM, J. Sci. Comput.*, **14** (2), pp. 483-505.

Bergmann M., Cordier L. and Brancher J.-P. (2003) Contrôle optimal par réduction de dynamique du sillage instationnaire d'un cylindre circulaire. *$16^{ième}$ Congrès Français de Mécanique, Nice, 1-5 septembre 2003.*

Bernal L.P.and Roshko A. (1986): Streamwise Vortex Structure In Plane Mixing Layers. *J. Fluid Mech.*, **170**, pp. 499–525.

Bertagnolio F. and Daube O. (1996): Velocity-vorticity formulation of the incompressible Navier-Stokes equations on non orthogonal grids. *Proceedings of the third ECCOMAS Computational Fluid Dynamics Conference*, p. 644.

Booker A.J., Dennis Jr. J.E., Frank P.D., Serafini D.B., Torczon V. and Trosset M.W. (1998): A Rigorous Framework for Optimization of Expensive Functions by Surrogates. *Icase report*, N°. 98-47. Downloadable in http://www.icase.edu/library/reports/rdp/1998.html.

Braza M., Chassaing P. and Ha Minh H. (1986): Numerical study and physical analysis of the pressure and velocity fields in the near wake of a circular cylinder. *J. Fluid Mech.*, **165**, 79.

Braza M., Chassaing P. and Ha Minh H. (1990): Prediction of large-scale transition features in the wake of a circular cylinder. *Phys. Fluids A*, **2** (8), pp. 1461-1471.

Cazemier W., Verstappen R.W.C.P. and Veldman A.E.P. (1998): Proper orthogonal decomposition and low-dimensional models for driven cavity flows. *Phys. Fluids*, **10**, (7), pp. 1685-1699.

Chorin A.J. (1968): Numerical solution of the Navier-Stokes equations. *Math. Comp.*, **22**, pp. 745-762.

Conn A.R., Gould N.I.M. and Toint P.L. (2000): Trust region methods. *SIAM*, Philadelphia.

Cordier L. (1996): Etude de systèmes dynamiques basés sur la décomposition orthogonale aux valeurs propres (POD). Application à la couche de mélange turbulente et à l'écoulement entre deux disques contra-rotatifs. *PhD dissertation, Poitiers university*, in french.

Cordier L. and Bergmann M. (2002): Proper Orthogonal Decomposition: an overview. *Lecture series 2002-04* on post-processing of experimental and numerical data, Von Karman Institute for Fluid Dynamics.

Cordier L., Delville J. and Tenaud C. (1997): Low dimensional description of large scale structures dynamics in a plane turbulent mixing layer. *Eleventh Symposium on Turbulent Shear Flows.*

Deane A.E., Kevrekidis I.G., Karniadakis G.E. and Orszag S.A. (1991): Low-dimensional models for complex geometry flows: Application to grooved channels and circular cylinders. *Phys. Fluids A*, **3** (10), pp. 2337-2354.

Delville J. (1994): Characterization of the organization in shear layers via the Proper Orthogonal Decomposition. *Applied Scientific Research*, **53**, pp. 263-281.

Delville J. (1995): La Décomposition Orthogonale aux Valeurs Propres et l'Analyse de l'Organisation Tridimensionnelle des Ecoulements Turbulents Cisaillés Libres. *PhD dissertation, Poitiers university*, in french.

Delville J., Ukeiley L., Cordier L., Bonnet J.-P. and Glauser M. (1999): Examination of large-scale structures in a turbulent mixing layer. Part 1. Proper Orthogonal Decomposition. *J. Fluid Mech.*, **391**, pp. 91-122.

Fahl M. (2000): Trust-Region methods for flow control based on Reduced Order Modeling. *PhD dissertation, Trier university.* Downloadable in http://www.mathematik.uni-trier.de:8080/~fahl.

Fletcher C.A.J. (1991): Computational techniques for Fluid Dynamics. *Springer-Verlag*, New York.

Gad-el-Hak M. (2000): Flow Control: Passive, Active and Reactive Flow Management. *Cambridge University Press*, London, United Kingdom.

Gad-el-Hak M. (2002): The MEMS Handbook. *CRC Press*, Boca Raton, Florida.

Gillies E.A. (1998): Low-dimensional control of the circular cylinder wake. *J. Fluid Mech.*, **371**, pp. 157-178.

Graham W.R., Peraire J. and Tang K.Y. (1999a): Optimal control of vortex shedding using low order models. Part 1: Open-loop model development. *Int. J. for Numer. Meth. in Engrg.*, **44** (7), pp. 945-972. Downloadable in http://raphael.mit.edu/pubs.html.

Graham W.R., Peraire J. and Tang K.Y. (1999b): Optimal control of vortex shedding using low order models. Part 2: Model-based control. *Int. J. for Numer. Meth. in Engrg.*, **44** (7), pp. 973-990. Downloadable in http://raphael.mit.edu/pubs.html.

Gunzburger M.D. (1995): Flow control. *Springer*, New York.

Gunzburger M.D. (2000): Adjoint eqaution-based methods for control problems in incompressible, viscous flows. *Flow, Turbulence and Combustion*, **65**, pp. 249-272.

He J.-W., Glowinski R., Metcalfe R.,Nordlander A. and Périaux J. (2000): Active control and drag optimization for flow past a circular cylinder. Part 1. Oscillatory cylinder rotation. *J. Comp. Phys.*, **163**, pp. 83-117.

Henderson R.D. (1997): Nonlinear dynamics and patterns in turbulent wake transition. *J. Fluid Mech.*, **352**, 65.

Hinze J.O. (1975): Turbulence. *McGraw-Hill*, New York, 2nd ed.

Homescu C., Navon I.M. and Li Z. (2002): Suppression of vortex shedding for flow around a circular cylinder using optimal control. Int. J. Numer. Fluids. **38**, Issue 8, pp. 43-69. Downloadable in http://www.csit.fsu.edu/ navon/pubs/index.html.

Iollo A. (1997): Remarks on the approximation of the Euler equations by a low order model. *INRIA research report n° 3329*. Downloadable in http://www.inria.fr/rrrt/rr-3329.html.

Iollo A., Lanteri S. and Désidéri J.-A. (1998): Stability properties of POD-Galerkin approximations for the compressible Navier-Stokes equations. *INRIA research report n° 3589*. Downloadable in http://www.inria.fr/rrrt/rr-3589.html.

Ito K. and Ravindran S.S. (1998): A reduced-order method for simulation and control of fluid flows. *J. Comp. Phys.*, **143**, pp. 403-425.

Jin J. and Braza M. (1993): A nonreflecting outlet boundary condition for incompressible unsteady Navier-Stokes calculations. *J. Comput. Phys.*, **107**, N° 2, pp. 239-253.

Joslin R.D., Gunzburger M.D., Nicolaides R.A., Erlebacher G., Hussaini M.Y. (1995): A Self-Contained, Automated Methodology for Optimal Flow Control Validated for Transition Delay. *ICASE Report 95-64*. Downloadable in http://www.icase.edu/library/reports/rdp/1995.html.

Lardat R., Bertagnolio F. and Daube O. (1997a): La formulation vitesse-tourbillon en maillage décalé : une méthode de projection. *C. R. Acad. Sci. Paris*, **t. 324**, Série II *b*.

Lardat R., Shen W.Z., Ta Phuoc L., Tenaud C.,Cordier L. and Delville J. (1997): Large Eddy Simulation of a spatially developing 3D shear layer in incompressible flow: comparisons with detailed experiments. *IUTAM-Symposium: Simulation and Identification of Organized Structures in Flows (SIMFLOW)*, TUD Lyngby, Denmark. SIMFLOW, pp. 447-456, Kluwer Academic Publishers.

Li Z., Navon I.M., Hussaini M.Y. and Le Dimet F.-X. (2002): Optimal control of cylinder wakes via suction and blowing. *Computers & Fluids*, **31**, Issue 8. Downloadable in http://www.csit.fsu.edu/ navon/pubs/index.html.

Morgan K. and Peraire J. (1998): Unstructured grid finite element methods for fluid dynanics. *Reports on Progress in Physics*, **61**, N° 6, pp. 569-638. Published by the Institute of Physics. Downloadable in http://raphael.mit.edu/pubs.html.

Prabhu R.D., Collis S. Scott and Chang Y. (2001): The influence of control on proper orthogonal decomposition of wall-bounded turbulent flows. *Phys. Fluids*, **13** (2), pp. 520-537.

Prandtl L. (1925): The Magnus effect and windpowered ships. *Naturwissenschaften*, **13**, 93.

Ravindran S.S. (2000a): Reduced-order adaptive controllers for fluid flows using POD. *J. of Scientific Computing*, **15**, N° 4, pp. 457-478.

Ravindran S.S. (2000b): A reduced-order approach for optimal control of fluids using proper orthogonal decomposition. *int. J. Numer. Meth. Fluids*, **34**, pp. 425-448.

Rempfer D. (1996): Investigations of boundary layer transition via Galerkin Projections on Empirical Eigenfunctions. *Phys. Fluids*, **8**, (1), pp. 175-188.

Rempfer D. and Fasel H.F. (1994): Evolution of three-dimensional coherent structures in a flat-plate boundary layer. *J. Fluid Mech.*, **260**, pp. 351-375.

Sagaut P. (1995): Simulations numériques d'écoulements décollés avec des modèles de sous-maille. *PhD dissertation, Paris VI university*, in french.

Sirovich L. (1987a): Turbulence and the dynamics of coherent structures. Part 1 :Coherent structures. Quarterly of Applied Mathematics **XLV**, N° 3, pp. 561–571.

Sirovich L. (1987b): Turbulence and the dynamics of coherent structures. Part 2 : Symmetries and transformations. Quarterly of Applied Mathematics **XLV**, N° 3, pp. 573–582.

Ta Phuoc L. (1994): Modèles de sous maille appliqués aux écoulements instationnaires décollés. eds. DGA/DRET, *Journée thématique DRET : Aérodynamique instationnaire turbulente - Aspects numériques et expérimentaux.*

Taylor G.I. (1932): The Transport of Vorticity and Heat through Fluids in Turbulent Motion. *Proc. of the London Math. Soc. Series*, **A 151**, p. 421.

Tokumaru P.T. and Dimotakis P.E. (1991): Rotary oscillatory control of a cylinder wake. *J. Fluid Mech.*, **224**, p. 77.

Ukeiley L., Cordier L., Manceau R., Delville J., Glauser M. and Bonnet J.-P. (2001): Examination of large-scale structures in a turbulent mixing layer. Part 2. Dynamical systems model. *J. Fluid Mech.*, **441**, pp. 67-108.

Zienkiewicz O.C. and Morgan K. (1983): Finite Elements and Approximation. *John Wiley*, New York.

Zienkiewicz O.C. and Taylor R.L. (2000): The Finite Element Method. *Butterworth and Heneimann*, 5th Edition.

Zhou X. and Sirovich L. (1992): Coherence and chaos in a model of turbulent boundary layer. *Phys. Fluids*, **4** (12), pp. 2855-2874.